

1
2
3
4
5
6
7
8
9
10
11
12
13
14
15
16
17
18
19
20
21
22
23
24
25
26
27
28
29
30
31
32
33
34
35
36
37
38
39
40
41
42
43
44

Re-examination of the Interstate 5 dust storm: Alternate interpretation of governing dynamics

Michael L. Kaplan¹, Ramesh K. Vellore^{1,2}, John M. Lewis^{1,3}, Patricia M. Pauley⁴,
Jonathan E. Martin⁵, R. Krishnan², and Matthew Young^{1,6}

Submitted to the *Journal of Geophysical Research (Atmospheres)*

22 September 2011

¹Division of Atmospheric Sciences, Desert Research Institute, Reno, NV 89512, USA.

²Center for Climate Change Research, Indian Institute of Tropical Meteorology, Pune 411 008, India.

³National Severe Storms Laboratory, Norman, OK 73072, USA.

⁴Naval Research Laboratory, Monterey, CA 93943, USA.

⁵Department of Atmospheric and Oceanic Sciences, University of Wisconsin, Madison, WI, 53706, USA.

⁶U.S. Navy, Fleet Weather Center, Fallon, NV 89496, USA.

Corresponding Author: Dr. Michael L. Kaplan, Division of Atmospheric Sciences, Desert Research Institute, 2215 Raggio Parkway, Reno, NV 89512, USA. Email:Mike.Kaplan@dri.edu.

45 **Abstract**

46 Over the Thanksgiving holiday of November 1991, a tragic set of automobile accidents
47 occurred in a dust storm that struck Interstate Highway 5 in California's San Joaquin Valley.
48 Meteorologists from the U. S. Naval Research Laboratory analyzed this storm in the mid-1990s.
49 In light of a recently published paradigm for dust storm generation over the western USA that
50 differs from the well-established Danielsen paradigm from the 1970s, this earlier research has
51 been re-analyzed with the benefit of a high-resolution mesoscale prediction model, the Weather
52 Research and Forecast (WRF) model. The new paradigm differs from the older paradigm in
53 several respects — most notably in regard to both space and time scale. The new paradigm
54 places emphasis on fast adjustment processes, adjustment of mass as opposed to momentum, and
55 smaller-scale but more intense vertical circulations about the jet (meso- β scale in contrast to
56 synoptic scale). Our simulation of this case points to fast geostrophic adjustment (the order of
57 6–12 h) as a central component of dust storm generation as opposed to the slower synoptic-scale
58 adjustment (24–48 h) associated with the Danielsen paradigm. And although there is some
59 influence on upper-level frontogenesis from the synoptic-scale balanced indirect circulation
60 about the jet (the Danielsen paradigm), it appears that the bifurcation of this front through the
61 action of an intense small-scale direct circulation pattern is crucial for development of the low-
62 level winds that ablate the dust from the valley floor.

63

64

65

66

67

68 **1. Introduction**

69 Edwin Danielsen established the primary paradigm for dust storm generation over the
70 western and mid-western United States of America (USA) in the early 1970s [*Danielsen* 1974].
71 This view stemmed from his earlier work that explored stratospheric-tropospheric exchange
72 through reliance on the potential vorticity conservation principle and the associated isentropic
73 trajectories (see *Danielsen* [1968] for a review). Indeed, the paradigm is strongly based on the
74 existence of a “tropopause fold” indicative of the extrusion of stratospheric air into the
75 troposphere. In the mid-1990s, the Danielsen paradigm was central to the study of the tragic dust
76 storm that led to a series of automobile accidents on Interstate Highway 5 (I-5) in California over
77 the Thanksgiving holiday of November 1991 [*Pauley et al.* 1996; abbreviated as ‘P96’ in the
78 subsequent text].

79 The meteorological fields used in the P96 study were based on products from a “research
80 mode” version of the U. S. Navy’s statistical interpolation method [*Barker* 1992]. Although this
81 methodology strived to incorporate mesoscale detail into the analyses through the combination of
82 background fields from a 6-h forecast using NORAPS [Navy Operational Regional Atmospheric
83 Prediction System; *Hodur* 1987; *Liou et al.* 1994] and operational upper-air and surface
84 observations augmented by automated aircraft wind observations, some of the important smaller-
85 scale features of the analyses have now fallen into question. The questions arose when these
86 smaller-scale features were compared and contrasted with: (1) analyses pertinent to this case
87 study that stemmed from the more recent mesoscale reanalysis dataset NARR [North American
88 Regional Reanalysis; *Mesinger et al.* 2006], and (2) mesoscale features in the vicinity of western
89 USA dust storms recently studied by *Lewis et al.* [2011] and *Kaplan et al.* [2011].

90 We re-examine the I-5 dust storm in this study with the benefit of a high resolution
91 numerical simulation from the Weather Research and Forecasting (WRF) model [*Skamarock et*
92 *al.* 2008]. The re-examination is justified on the basis of the recent studies of *Lewis et al.* [2011]
93 and *Kaplan et al.* [2011] that have established another view or paradigm of dust storm generation
94 over the western USA. In this newer paradigm, mesoscale processes are emphasized in addition
95 to the synoptic scale processes germane to the Danielsen view.

96 The key features or signatures that differentiate the old and new paradigms are the
97 following: (1) the new paradigm places emphasis on fast adjustment processes where the mass
98 field dominates the adjustment process as opposed to slower momentum adjustment in the
99 Danielsen view, and (2) the new paradigm indicates that the crucial vertical circulations about
100 the upper-level jet streak are unbalanced large-magnitude direct circulations on the mesoscale as
101 opposed to the balanced (quasi-geostrophic; Q-G) indirect circulations on the synoptic scale in
102 the Danielsen paradigm.

103 After a description in section 2 of the WRF model and the design of experiments to
104 explore dust storm generation, section 3 contains an overview of the dust storm originally
105 discussed in P96. Sections 4 and 5 provide comprehensive mesoscale analyses of the event with
106 comparison and contrast to the P96 contribution where appropriate. A summary and discussion
107 of research results are found in the final section 6.

108 **2. Model setup and simulation**

109 The high-resolution numerical simulation presented in this paper is conducted using the
110 Weather Research and Forecasting (WRF) model [*Skamarock et al.* 2008]. The modeling setup
111 considered in this study was primarily focused on the target region of California and Nevada
112 with the WRF modeling domains shown in Figure 1. The interactive strategy between the model

113 domains was one-way. The model configuration had 47 levels in the vertical extending up to 15
114 km AGL with 18 vertical levels below 1.5 km AGL and with the lowest model level set at 10 m
115 AGL. The model physics included: (i) momentum and heat fluxes at the surface computed using
116 an Eta surface layer scheme [Janjić 1996, 2001] following Monin-Obukhov similarity theory, (ii)
117 turbulence parameterization following the Mellor-Yamada-Janjić 1.5 order (level 2.5) turbulence
118 closure model [Mellor and Yamada 1974, 1982; Janjić 2001], (iii) convective processes
119 following the Betts-Miller-Janjić cumulus scheme [Betts 1986; Betts and Miller 1986; Janjić
120 1994], (iv) cloud microphysical processes following explicit bulk representation of microphysics
121 [Thompson *et al.*, 2004, 2006], (v) radiative processes parameterized using the Rapid Radiative
122 Transfer Model for long wave radiation [Mlawer *et al.* 1997] and the Dudhia short wave scheme
123 [Dudhia 1989].

124 Land-surface processes were parameterized following the Noah land surface model
125 (Noah LSM) which provided the surface sensible, latent heat fluxes, upward longwave and
126 shortwave fluxes to the atmospheric model [Chen and Dudhia 2001; Ek *et al.* 2003]. High-
127 resolution (30" arc resolution) datasets of topography, land mask, land use, and soil type
128 archived by the United States Geological Survey (USGS) were used as static fields in the
129 simulation. The USGS topography is shown in Figure 2.

130 The NARR dataset provided the initial and boundary conditions to WRF. This dataset is a
131 3-hourly high-resolution reanalysis that covers North America produced by the National Center
132 for Environmental Prediction (NCEP) Eta model (32 km grid spacing and 45 layers) together
133 with the Regional Data Assimilation System (RDAS) [Mesinger *et al.* 2006]. The WRF model
134 was initialized at 1200 UTC 28 November 1991. Figure 2 shows cross sections used in this
135 study to examine the vertical structure of the atmosphere. They are: southwest-northeast oriented

136 cross-sections J-J' [passing through Oakland (OAK), South Lake Tahoe (TVL), California and
137 Fallon (NFL), Nevada], K-K' [passing through the San Joaquin Valley north of Fresno (FAT)
138 and Coalinga (COA) in California], and a nearly north-south oriented cross section L-L'
139 extending from Vandenberg (VBG), California to Smoky Creek and Black Rock Deserts (BRD)
140 in northwestern Nevada passing through the I-5 accident site

141 **3. Synoptic overview and observations**

142 The meteorological conditions associated with the dust storm event of 29 November 1991
143 were detailed in P96 and are summarized here as background for the current study. This storm is
144 notorious for the sequence of collisions on I-5 [the main north-south Interstate highway in
145 California, extending northward from San Diego (NKX) and Los Angeles (LAX) [surface and
146 upper-air stations and their identifiers referenced in this study are listed in Table 1] through the
147 San Joaquin and Sacramento Valleys [Figure 2] that involved 164 vehicles with 17 fatalities and
148 151 people injured. On this date, blowing dust reports were widespread in California, not only in
149 the San Joaquin Valley in the vicinity of I-5, but also in the Salinas Valley [extending southeast
150 from Salinas (SNS) nearly to Paso Robles (PRB)] to its west, in the Mojave (see Figure 2) to its
151 southeast, and along California's South Coast. Even so, the visibility restrictions were the worst
152 in the central San Joaquin Valley (cf. Table 1 of P96). Of the stations listed in Table 2, Lemoore
153 Naval Air Station (NLC) was the closest geographically to the accident site and had the worst
154 conditions on this date with visibility less than 1 km for more than 2 hours around the time of the
155 I-5 accident. However, AVHRR satellite imagery (cf. Figure 4 in P96) shows two distinct dust
156 plumes in the San Joaquin Valley at 2204 UTC 29 November 1991 — one along the western side
157 of the valley affecting I-5, and another in the center of the valley affecting NLC.

158 Surface winds at the time of the accidents (2130–2240 UTC 29 November 1991) were
159 predominantly northwesterly and quite strong, with sustained winds at many stations of 10 m s^{-1}
160 or more and some gusts exceeding 20 m s^{-1} (Table 2). The winds were highly ageostrophic, with
161 an orientation nearly perpendicular to the sea-level isobars. Dew point temperatures at many
162 stations experienced an abrupt decrease that occurred earlier in the Sacramento Valley to the
163 north and later in the San Joaquin Valley to the south. Notably the surface observations at FAT
164 between 2200 UTC 29 November 1991 and 0000 UTC 30 November 1991 showed a rapid shift
165 in temperature from warming to cooling and a sudden drop in dew point temperature from -2°
166 to -17° C , the surface pressure shifts from falls to rises, and the wind direction shifts from
167 northwest to north-northeast. To the west and south of FAT, however, there is less of a signal of
168 this cool air surge with diurnal temperature changes more dominant.

169 P96 did not examine surface data for Nevada, where reduced visibilities and strong gusty
170 surface winds were observed north and east of Reno (REV) as early as 1130 UTC 29 November
171 1991 — 10 hours before the strong gusts in the Central Valley of California. The time sequence
172 of the onset of gusty winds and reduced visibilities from Winnemucca (WMC), Nevada to TVL
173 occurred between 1130 and 2130 UTC 29 November 1991 (Table 2). This indicates the
174 likelihood of surface adjustment to the upper-level forcing that propagated over the Sierra
175 Nevada Mountain Range (see Figure 2) just before the onset of the high surface winds in the
176 Central Valley of California that were associated with the I-5 dust storm.

177 The upper level flow field associated with the I-5 dust storm is best described as a large
178 amplitude synoptic-scale wave with an embedded jet streak. The NARR reanalyzed 500 hPa
179 wind speeds, temperature and geopotential height fields at 1200 UTC 29 November 1991 (10
180 hours prior to dust storm generation in the Central Valley of California) are shown in Figure 3.

181 A strong jet streak with a wind speed maximum of 55 m s^{-1} is located over southwestern Oregon
182 (OR; see Figure 1 for the state identifier) where its exit region extends from the northern to
183 central Sierra Mountain Range. A cold trough was just beginning to amplify over southeastern
184 Oregon and northwestern Nevada (NV) at this time, accompanied by an extreme southwesterly
185 directed temperature gradient of $0.02^\circ\text{K km}^{-1}$ extending from eastern Oregon to northern central
186 California (CA). Also, at this time the downward extension of the dynamic tropopause is
187 approximately crossing over the U.S. and Canada border region near eastern Washington (WA).

188 The tropopause pressure diagnosed from NARR at 0600 and 1800 UTC 29 November
189 1991 is shown in Figure 4. NARR diagnoses tropopause pressure through a surface-up search in
190 a model sounding where the first occurrence of three adjacent layers over which the lapse rate is
191 less than 2 K km^{-1} . The mid-point of the three layers is defined to be the tropopause. In addition
192 there is a lower bound of 500 hPa enforced on the tropopause pressure in the NARR diagnosis.
193 The lowest extension of the tropopause pressure for this case is 420 hPa which is located within
194 the jet streak's left entrance region and it continues to propagate southwards during 1200–1800
195 UTC 29 November 1991. A secondary weak perturbation to the tropopause pressure develops
196 west of the Sierra Nevada Range and over the Central Valley of California during this time. This
197 secondary perturbation feature provides evidence of a possible formation of a new baroclinic
198 zone above the region of dust storm formation.

199 The core of high momentum shrinks in time as the curvature of the system intensifies
200 between 1500 and 2100 UTC 29 November 1991 (Figures 5 and 6). A local increase in kinetic
201 energy occurs over and downstream of the southern Sierra Nevada Range. The 30 m s^{-1} isotach
202 propagates from the northern part of the Central Valley of California to western New Mexico
203 (NM) in less than 9 hours, indicating substantial advection of kinetic energy while the cold

204 trough strengthens over western Nevada and the central Sierra Range south of REV by 2100
205 UTC 29 November 1991. Clearly the distance between the amplifying cold trough and the
206 downstream gradient of kinetic energy within the jet's exit region is significantly increasing over
207 a time period less than 12 hours. One can also notice that the mid-tropospheric jet and height
208 fields are shifting their relative positions during 1500–2100 UTC 29 November 1991 (Figures 5
209 and 6). That is, the cross-jet height gradient (5700 - 5580 m isolines) increases between FAT
210 and the central California coast. The core of jet momentum shifts southwestwards closer to the
211 region of stronger northeast-southwest height gradient during this time. This reflects primarily in
212 700 hPa cooling (not shown) on the right side of the jet exit region, *i.e.*, 6-8°C cooling from
213 southeast of Edwards Air Force Base (EDW) to north of FAT at 700 hPa during this period. This
214 cooling reduces the 1000–500 hPa thickness resulting in height falls of larger magnitudes to the
215 northeast along a line from SAC to Bakersfield (BFL) during the time just before the accidents.
216 This increases the negative height gradient directed northeast to southwest across the accident
217 location. In short, the height gradients and jet are not in phase (getting back to phase) at 1500
218 UTC (2100 UTC) 29 November 1991 in the curved exit region. Also, notice that the 800 hPa
219 wind flow accelerates from the north and north-northeast during this time period between the
220 central California coast, SAC and just west of BFL. The accidents occur after 2200 UTC 29
221 November 1991 within this adjustment zone just west-southwest of FAT (see Figure 2).

222 **4. Lagrangian parcel motions**

223 We first examine this case study using parcel backtrajectory analyses. Figure 7 shows the
224 plan view of a backtrajectory of an air parcel reaching 900 hPa above FAT at 2300 UTC 29
225 November 1991. It should be noted that this trajectory is very similar to those starting farther
226 southwest coincident with the multiple accident location described earlier. The corresponding

227 parcel diagnostics along the backtrajectory are shown in Figure 8. It is seen that the parcel was
228 located at 600 hPa over British Columbia, Canada, (north of WA) at 0000 UTC, over central
229 Washington and eastern Oregon west of upper-air stations Spokane (OTX), Washington, and
230 Boise (BOI), Idaho, during 0600–1200 UTC, over northwestern Nevada west of Elko (LKN),
231 Nevada, at 1200 UTC, and over Lovelock (LOL), Nevada, at 1500 UTC 29 November 1991.
232 Parcel accelerations ($0.003 - 0.006 \text{ m s}^{-2}$) are significant just south of REV and north of Bishop
233 (BIH), California during 1800–2100 UTC 29 November 1991 (Figure 8). That is, the parcel is
234 generally decelerated on the left side of the jet until 1800 UTC 29 November 1991. Then the
235 parcel explosively accelerated just south of REV over the Sierra Nevada with a pronounced
236 ageostrophic wind component and pressure jump directed to the south as it descends down the
237 Sierra Nevada and turns right into the Central Valley of California. Furthermore, it is during this
238 period of acceleration down the Sierra Nevada, *i.e.*, approaching 2100 UTC, the parcel
239 diagnostics in Figure 8 indicate that surface sensible heat flux, PBL depth and TKE increases
240 rapidly and the Richardson number rapidly decreases to zero.

241 As the air parcel approaches the region L-L' along the trajectory path (see Figure 2 for
242 the orientation of this cross section) the northerly wind component increases at 900 hPa just
243 north-northeast of COA, *i.e.*, over FAT which closely coincides with the I-5 accident location at
244 2200 UTC 29 November 1991. The parcel acceleration and turning of the wind in the 950–800
245 hPa layer provides evidence for the increasing northerly momentum available for mixing
246 surfaceward by 2200 UTC 29 November 1991. The source of this momentum is the strong south-
247 southwestward-directed ageostrophic wind accompanying the cold air moving over and down the
248 central Sierra Nevada. The descent of the parcel is closely coupled to the strongest terrain
249 gradients as can be seen in Figure 8.

250 Parcel diagnostics indicate that there is very little net subsidence in air parcels that enter
251 the region of dust storm formation. To better understand what type of circulation produces this
252 transport regime, we performed a thorough diagnosis isolating the relative balance or imbalanced
253 state of the parcel motions and their effects on the dust storm generation environment.

254 **5. Diagnoses of multi-scale adjustment processes**

255 The synthesis of multi-scale interactions for the likelihood of dust storms follows the
256 work of *Lewis et al.* [2011] and *Kaplan et al.* [2011]. Before describing the imbalance in this
257 case study, we specifically define this concept. By imbalance, we mean a sequence of processes
258 that interrupt Q-G circulations in conjunction with thermal wind balance. This sequence begins
259 with a difference between the advection of total wind and geostrophic wind in the exit region of
260 a jet streak. This difference or separation disrupts the weakly accelerative or “balanced” Q-G
261 circulations that maintain thermal wind balance. The more curved the flow, the stronger the
262 inertial advection and the stronger the cross-stream pressure gradient within the exit region,
263 dominated by thermally direct circulations. That is, the requirement for accelerative flow to
264 redistribute the mass rather than decelerative flow to redistribute the momentum in the exit
265 region.

266 The changing mass rather than momentum field is the focal point of this adjustment
267 process characterized by short adjustment periods [*Kaplan et al.* 2011] as opposed to longer
268 space- and time-scale accompanying momentum adjustments [*Danielsen* 1974].

269 **5.1 Imbalance diagnostics**

270 **5.1.1 Thermal wind imbalance (meso- α scale)**

271 Rawinsonde soundings from BOI, WMC, and Salem (SLE) (see Table 1, Figures 2 and 7
272 for their locations; soundings not shown) gave evidence of a pronounced stable layer between

273 700 and 600 hPa with a mean static stability of 5.8 K km^{-1} at 0000 UTC 29 November 1991.
274 This stable layer was associated with strong warm air advection from the west-northwest.
275 Although there was evidence of veering near the base of this layer, there was no veering within
276 this layer – inconsistent with geostrophic theory. In essence, this case exhibited substantial
277 thermal wind imbalance.

278 From a sub-synoptic scale perspective, the precursor signals in the jet exit region of this
279 case share common features with those discussed in *Lewis et al.* [2011] and *Kaplan et al.* [2011].
280 We first bring attention to the jet exit regions – one associated with the total wind and the other
281 with the geostrophic wind. Isotachs of 30 m s^{-1} are used to designate these regions. The distance
282 separating these exit regions increases from 100 to 400 km over a period of 6 hours. The
283 separation occurs over southeastern California, southeastern Nevada, Arizona and western New
284 Mexico (Figures 5 and 6; see Figure 1 for state identifiers). This separation marks the
285 strengthening of the kinetic energy in the total wind jet exit region downstream from a
286 weakening jet core. This is not consistent with the balanced Q-G dynamics following parcel
287 decelerations under the influence of Coriolis force [*Danielsen 1974; Uccellini and Johnson*
288 *1979*]. That is, the wind and height fields in the jet exit region are out of balance on the meso- β
289 scale in the vicinity of observed dust storm activity. This is in response to a substantial difference
290 between the horizontal advection of the geostrophic momentum and the horizontal advection of
291 the total wind momentum over California. Further, this is reflected in the wind/height geometry
292 in the jet exit region that shows a separate total wind maximum in a region where the cross-
293 stream height gradient has strengthened. This is especially apparent over western Arizona by
294 2100 UTC 29 November 1991 and reflects the juxtaposition of the adiabatic cooling both ahead
295 of and on the left side of the jet with the advection of momentum by the total wind over

296 southeastern California, southeastern Nevada as well as western Arizona between 1500 and 1800
297 UTC 29 November 1991 (see also Figure 8 and explanation in *Lewis et al.* [2011]).

298 Furthermore, while the imbalance intensifies between wind and mass in the jet exit
299 region, the core of the jet weakens reflecting this downstream adjustment to sub-geostrophic
300 curved flow. The maximum cross jet height gradient has shifted downstream in response to the
301 curvature-induced thermally direct circulation as described in *Lewis et al.* [2011]. In effect a new
302 entrance region of the geostrophic wind jet forms where the curvature in the total wind jet's exit
303 region has maximized.

304 The aforementioned spatial separation between geostrophic and total wind jets is a
305 measure of thermal wind imbalance due to curvature effects. The region of interest for the initial
306 signs of thermal wind imbalance is bounded by the stations Sacramento (SAC), REV, and FAT.
307 The total wind and thermal wind vectors during the period 1200 – 1800 UTC 29 November 1991
308 are shown in Figure 9. There is unambiguous evidence of thermal wind imbalance in the 700-500
309 hPa layer over this region of interest. As mentioned above, the total wind shear propagates
310 downstream faster than the thermal wind shear. The total wind shear over the Sierra Nevada is
311 weaker than the thermal wind and this sub-geostrophy strengthens in time over this region,
312 particularly over the central Sierra Nevada. The thermal shear vector indicates a north-
313 northwesterly shear strengthening to greater than 50 m s^{-1} by 1800 UTC 29 November 1991 over
314 the Sierra Nevada between REV and FAT while the total wind vector is becoming much weaker.
315 The thermal wind vector begins to increase its magnitude in this region but its direction is not
316 consistent with the total wind shear vector. The thermal wind exhibits strong backing by 1800
317 UTC after a dominance of veering before 1200 UTC 29 November 1991.

318 To summarize, a major departure from geostrophic balance exists due to a lag in the mass
319 adjustment to the wind field. This lag is the result of an early veering thermal wind and
320 subsequent thermal wind adjustment towards balance through backing. Early on, the total wind
321 veers too little as geostrophic veering due to warm air advection is large compared to the total
322 wind shear. Later, backing occurs in the adjusting thermal wind as the mass field adjusts to the
323 total wind. As will be seen later, the thermal wind backs in response to ascent-induced cooling in
324 the cyclonic geostrophic exit region thereby allowing the thermal wind backing to become larger
325 than the total wind backing. Clearly this adjustment location is a region of rapidly evolving
326 ageostrophic flow where the total wind shear is less than the geostrophic wind shear consistent
327 with subgeostrophy in the curved jet exit region.

328 ***5.1.2 Ageostrophy – Lagrangian Rossby number (meso- β scale)***

329 The ageostrophic wind vectors at 500 hPa for this case are shown in Figure 10. There is a
330 progression/rotation of the ageostrophic vector that is initially oriented upstream against the jet
331 and subsequently cross-stream of the trough axes. This change in orientation of the vector,
332 initially opposed to the advection of kinetic energy, is consistent with the sub-geostrophy in the
333 trough followed by a left turn of the geostrophic wind. The progression is also consistent with
334 the flow approaching gradient wind balance in time followed by more unbalanced meso- β scale
335 flow where the leftward-directed ageostrophic flow controls the backing vertical shear through
336 inertial-advective processes [Lewis *et al.* 2011]. This evolution can be seen in Figure 10 where
337 the strongest ageostrophic vectors are north and northwest of REV, northeastern California and
338 southeastern Oregon at 1200 UTC 29 November 1991, and then they propagate southward over
339 the Sierra Nevada towards the region extending from just northeast to southeast of FAT by 2100
340 UTC 29 November 1991. The primary vector direction is northwestwards with a gradual turning

341 northwards between FAT and the region east of BFL as time progression passes. This turning
 342 reflects a dominance of subgeostrophy in the geostrophic exit region followed by a rotation
 343 towards the cyclonic/cold side of the jet.

344 These mesoscale regions of extreme ageostrophy are also evident in Figure 11 through
 345 diagnosed Lagrangian Rossby numbers (Ro^L), defined as follows:

$$346 \quad Ro^L = \left| \frac{\partial \vec{V}_H}{\partial t} + \vec{V}_H \cdot \nabla \vec{V}_H \right| / f |\vec{V}_H| \quad (1)$$

347 (see Appendix A for the definition of variables). $Ro^L \geq 0.5$ is referred to as the high Rossby
 348 number regime [Van Tuyl and Young 1982; Zack and Kaplan 1987; Koch and Dorian 1988;
 349 O'Sullivan and Dunkerton 1995; Kaplan et al. 1997, 1998; Hamilton et al. 1998; Zhang et al.
 350 2002; Kaplan et al. 2011].

351 The Lagrangian Rossby numbers for this case at 1500 UTC and 1800 UTC 29 November
 352 1991 are shown in Figure 11. The high Ro^L signal (≥ 0.5 and in certain locations exceeding 1.0)
 353 moves from north of REV to the southeast of FAT by 1800 UTC 29 November 1991. This
 354 indicates the existence of a state of mass/momentum imbalance and associated acceleration of
 355 the flow. Where ageostrophy is large, accelerations are large and oppose the balanced flow in the
 356 jet exit region. Additionally, the vertical wind shear deviates from thermal wind balance. This
 357 imbalanced state is a precedent for dust storm development. The high Rossby number signal
 358 propagates from the Sierra Nevada to south of FAT.

359 **5.1.3 Divergence diagnostics**

360 The meso- β scale regions of mass imbalance are further diagnosed through the velocity
 361 divergence budget aloft. The material derivative of horizontal velocity divergence (δ) on a
 362 sphere (using pressure as the vertical coordinate) is written as follows:

363
$$\frac{d\delta}{dt} + \delta^2 - R_\omega = f\zeta - u\beta + 2 \left[J(u, v) - \left(\frac{1}{r_e \cos \varphi} \right) \frac{\partial}{\partial \varphi} \left(\frac{u^2 + v^2}{2} \sin \varphi \right) \right] - \nabla^2 \Phi \quad (2)$$

364 The terms in equation (2) are defined in Appendix A.

365 In this case study we focus on the region near the I-5 accident location between 1800 and
 366 2300 UTC 29 November 1991. The 500 hPa diagnosed divergence budget of the terms in
 367 equation (2) at 37°N, 120.4°W along with the column-integrated mass flux divergence during
 368 1200 UTC 29 November 1991 – 0000 UTC 30 November 1991 are shown in Table 3. As the
 369 period and location of high Ro^L approaches this location (~1800 UTC), positive divergence
 370 tendencies develop and create upward vertical motions across the jet exit region with an
 371 unbalanced thermally direct circulation on the right side. The increasing upward motion
 372 enhances the adiabatic cooling, and by 2100 UTC 29 November 1991 the adiabatic cooling
 373 rapidly forces the hydrostatic heights to fall (*i.e.*, $-\nabla^2 \Phi < 0$). This effectively controls the shift
 374 from positive to negative divergence tendencies in combination with the tilting term. This also
 375 indicates that increasing mass flux convergence aloft in this region leads to surface pressure
 376 perturbations, *i.e.*, increasing local surface pressure tendencies. The column-integrated mass flux
 377 divergence indicated a surface pressure rise of about 1 mb hr⁻¹ at and later than 2100 UTC 29
 378 November 1991.

379 The shift of divergence to convergence tendencies is most apparent after 1800 UTC 29
 380 November 1991 northeast and near FAT (Table 3). The positive divergence tendencies peak at
 381 1900 UTC 29 November 1991 and then become sharply negative by 2300 UTC 29 November
 382 1991. This is consistent with the period of shift from ascent to descent west of FAT. By creating
 383 the convergence tendencies and adiabatic cooling, the geostrophic jet becomes more cyclonic
 384 thus changes the advection of geostrophic wind through the trough region. The

385 confluence/difffluence structure enables the mass field advection to catch up with the wind field
386 advection accompanying the early-stage thermal wind imbalance. In the next section we will
387 provide evidence for the unbalanced signal in the vertical motion field consistent with the rapid
388 changes in Lagrangian divergence tendencies.

389 ***5.2 Vertical motion***

390 As seen earlier, the unbalanced ascent is the result of the development of velocity
391 divergence which shifts in time to the right side of the jet's exit region in the high Rossby
392 number zones. As will be seen later, when these adjustments become collocated with surface
393 sensible heating, the strongest buoyant and shear generation of turbulence kinetic energy (TKE)
394 occurs.

395 The simulated vertical p -velocity (ω on an isobaric surface; referred as the total ω -field in
396 the following text) and diagnosed ω using the simulated velocity and thermodynamic fields
397 following the Q-G approach [equation 5.6.11 from *Bluestein* 1992; *Martin* 2006, p.162],
398 horizontal winds and isentropes along the cross sections J-J' and K-K' (see Figure 2 for the
399 location of these cross sections) are shown in Figures 12 – 15. Notice the differences between the
400 total ω and Q-G ω along the northern side (between TVL and NFL) of the cross section at 1500
401 UTC 29 November 1991. As the wind and height field become unbalanced in the propagating
402 exit region, one can see the development of a strong ascending plume, at approximately 475 km
403 along the J-J' cross section, three times the magnitude of the diagnosed Q-G plume (Figure 12).
404 The total ω -plume is directly under the right side of the southwestward-shifted geostrophic jet
405 (J_g) at 1500 UTC.

406 However, the total ω is markedly different from its Q-G counterpart at 1800 UTC 29
407 November 1991 (Figures 14 and 15). The ascending plume is nearly co-located with the large

408 Rossby number regime near under the southwestward-shifted total wind jet (J ; not to be
409 confused with the indexing of the cross-section) and above the western side of the Sierra Nevada
410 (Figure 14). Also, the Q-G ω 's indicate a balanced thermally indirect circulation and leeside
411 orographic descent at this time (Figure 15). The likelihood of this ascending plume at 1800 UTC
412 29 November 1991 in the total ω field being forced primarily by Q-G processes is strongly
413 diminished by virtue of the simulated high Rossby numbers and derived Q-G descent. In spite of
414 slight orographic descent as a component of the wind flow which moves from north to south
415 down the Sierra Nevada, it is also remarkable to notice the prevalence of this unbalanced ascent
416 on the western slope of the mountains northeast of FAT that compensates for the anticipated
417 orographic descent. This location is critical to storm development.

418 Additionally, as can be seen in Figures 13 and 15, J and J_g bifurcate over the Sierra
419 Nevada between 1500 and 1800 UTC 29 November 1991 and shift their relative locations –
420 indicative of complex differences in mass and momentum advection. Again, this bifurcation is
421 reflective of the advection of mass and momentum differences and is the reason for the complex
422 mutual adjustment processes. The bifurcation is so critical and cannot be resolved by the coarse
423 analyses of the Navy Operational Regional Atmospheric Prediction System [NORAPS; *Liou et*
424 *al.* 1994] employed in P96.

425 ***5.3 Cold frontal structure***

426 Consistent with the upward-stretched isentropes seen in Figure 14 at 1800 UTC 29
427 November 1991 (just west of the 400 km location), one can see the cooling signal building
428 towards the southwest over the Sierra Nevada in the diagnosed 700–500 hPa hydrostatic layer
429 mean temperatures between 1200 and 1800 UTC 29 November 1991 (Figure 16). This cooling is
430 consistent with mid-tropospheric ascent along the northeast-southwest cold tongue that builds

431 through this period from south of REV to east of BFL as diagnosed from the simulated thermal
432 boundary/front between -14°C and -20°C in this region. This boundary strengthens and is
433 crossing under the jet by 1800 UTC 29 November 1991 relative to its location at 1200 UTC over
434 northwestern Nevada. At 700 hPa the cold pool actually propagates southeastwards from east of
435 SAC to near BFL.

436 Also, the simulated WRF soundings between COA and EDW during 1800 UTC 29
437 November 1991 – 0000 UTC 30 November 1991 indicated that the depth and intensity of the
438 adiabatic layer increases between the surface and mid-troposphere as one moves east and
439 southeastward from the I-5 accident site (see Figure 2 for the location). The NLC and BFL
440 simulated soundings in Figure 17 between COA and EDW show strong cooling signatures. The
441 strengthening mid-lower tropospheric temperature boundary is reflected in the magnitude of
442 temperature decrease in the 1000–700 hPa layer between COA and EDW. Consistent with the
443 region of observed blowing dust, the 700 hPa temperature drop of 4°C (10°C) at COA (EDW)
444 juxtaposed with rising surface temperatures create a near-neutral PBL in the southern part of the
445 San Joaquin Valley during this period.

446 Further analysis of additional model soundings and vertical cross sections farther south
447 between the San Joaquin Valley and the Sierra Nevada (not shown here) indicated that 700 hPa
448 cooling is more intense in the region surrounded by the stations EDW-BFL-FAT before and
449 during dust storm genesis. This is because there are two short period and substantial waves of
450 adiabatic cooling, one in the balanced curved flow ahead of the trough between 1800 and 2100
451 UTC in the region BFL-BIH-EDW and a second within the unbalanced right exit region between
452 1500 and 2100 UTC that rapidly propagates southward from REV to east of BFL. These two
453 waves of cold air merge at 2100 UTC 29 November 1991 between BFL and EDW. As the

454 warmer surface air north-northeast of COA moves southward it undercuts the two merging cold
455 pools building from 1) east-northeast to southwest and 2) north to south primarily in the region
456 FAT-BFL-EDW by 2200 UTC 29 November 1991.

457 It should be mentioned that the accidents on I-5 referenced in P96 correspond to the
458 strong winds and dust stream from the regions where the cold air is undercut by an initial warm
459 plume at the surface, i.e., predominantly northeast of COA and not just from the locations where
460 the coldest air aloft and the deepest adiabatic layer is seen. One can see that the surface heats up
461 more at NLC while the 700 hPa cooling is greater at BFL between 1800 UTC 29 November
462 1991 and 0000 UTC 30 November 1991 (Figure 17). This region between NLC and BFL is
463 where the initial Q-G cold front aloft is bifurcated into two fronts with the southern front having
464 a mesoscale structure. The San Joaquin Valley is the location of the juxtaposed cold air
465 propagating southward and westward in the lower-mid-troposphere and warm near-surface air
466 propagating south-southeastwards. WRF indicates that it is just as cold in between BFL and
467 EDW as it is at FAT which explains the broad eruption of dust from east to west across the San
468 Joaquin Valley as opposed to north to south as observed by P96.

469 ***5.4 Surface pressure perturbations and PBL turbulence***

470 The unbalanced ascent not only stretches the isentropes under the jet but also increases
471 the kinetic energy from the low-level mass adjustments. That is, the ageostrophic flow will
472 generate divergence early on thus supporting a downstream propagation of a surface low
473 pressure center. However, the unbalanced cooling and shift of cold air across the jet will
474 compensate by forcing the surface pressure to rise immediately behind the low-level pressure
475 falls [see also Table 3; and *Cram et al.* 1991; *Karyampudi et al.* 1995a].

476 Such features are seen in the diagnoses of sea-level pressure tendency and isallobaric
 477 wind (Figure 18), specifically: (i) the narrow plume of very strong mean sea level pressure rises
 478 ($> 3 \text{ mb hr}^{-1}$) coming over the Sierra Nevada from east of REV to FAT during 1500 – 1800 UTC
 479 29 November 1991 and then south and west of FAT between 1800 and 2100 UTC 29 November
 480 1991 ($> 3 \text{ mb h}^{-1}$) and (ii) the strong gradient from west to east of these pressure rises across the
 481 Central Valley of California in concert with the cold pool aloft within the 700 – 500 hPa layer in
 482 the same region (Figure 16). This is indicative of the low-level mass adjustments that are coupled
 483 to the cold pool building southwestwards near the unbalanced ascent over the central Sierra
 484 Nevada.

485 The isallobaric part (\vec{V}_{is}) of the ageostrophic wind [*Bluestein* 1992; *Martin* 2006;
 486 *Rochette and Market* 2006] is given by:

$$487 \quad \vec{V}_{is} = -\frac{1}{\rho f^2} \nabla_z \left(\frac{\partial P_{MSL}}{\partial t} \right) \quad (3)$$

488 where ρ is the air density and P_{MSL} is the mean sea level pressure (see also Appendix A for the
 489 details of variables). The simulated low-level mass flux convergence is likely enhanced over the
 490 Central Valley of California by the development of the south-southwesterly-directed
 491 ageostrophic wind late in the aforementioned sequence of events. Notice that the
 492 southwestward-directed isallobaric wind vectors are located over the Central Valley of California
 493 by 1800 UTC 29 November 1991 (Figure 18) and below the unbalanced cold pool at mid-levels.
 494 That is, as the cold air builds southwestward it creates the unstable layer and pressure rises
 495 necessary for the isallobaric ageostrophic wind that creates low-level TKE between FAT and
 496 COA. The simulated TKE, winds and isentropes along cross section L-L' at 1800 and 2200
 497 UTC 29 November 1991 are shown in Figures 19 and 20. The maxima of TKE develop at two

498 locations. One above the highest upstream elevation and the second over and downstream from
499 the locations of very strong dust storm formation, *i.e.*, near COA. The downstream surge of TKE
500 develops in a region with accelerating surface flow from the north-northwest. The low-level
501 accelerating flow is associated with sensible heating at the surface, near-neutral isentropes as
502 well as developing mean sea level pressure rises and low-level isallobaric ageostrophic winds.

503 Near COA the developing north-northwesterly surface flow is consistent with the cooling
504 aloft and the mean sea level pressure rises. This occurs as the PBL winds slowly back from
505 northwest to north. The intensifying low-level kinetic energy is a response to the increase in
506 backing thermal winds as the mass field rapidly adjusts towards the momentum field under the
507 unbalanced conditions (cooling in the jet). The combination of unbalanced cooling, low-level
508 isallobaric winds and surface heating control the regions of strong turbulence to organize the dust
509 storm between COA and FAT. Notice the shift of isentropes in the 700–950 hPa layer northeast
510 of COA between 1800 and 2200 UTC 29 November 1991 (Figures 19 and 20). The shift occurs
511 as colder air is advected in from the north by the accelerating flow between 900 and 700 hPa.

512 The diagnosed mean sea level pressure signals also confirm the development of rises just
513 upstream of the dust storm locations (not shown here), *i.e.*, at REV, LOL, RDD, MCE, FAT,
514 COA and BIH (see station locations in Figure 2) during 1200–1900 UTC 29 November 1991.
515 Maximum mean sea level pressure rise of 10 hPa is seen at REV and BIH in 6 hours while the
516 rises at MCE, FAT and COA is about 2 hPa.

517 ***5.5 Schematic of adjustments***

518 A schematic diagram with adjustments following the newer paradigm of dust storm
519 generation recently documented in *Lewis et al.* [2011] and *Kaplan et al.* [2011] is shown in
520 Figure 21. The adjustment signals S1-S8 propagate from north-northeast to south-southwest

521 across the Sierra Nevada Mountain Range towards the dust storm locations in the Central Valley
522 of California. The processes for dust storm formation depicted in this schematic differ in many
523 ways from the analyses of P96. The analyses distilled in this study are consistent with a fast
524 adjustment process in a high Rossby number regime that occurs over 6–9 h as opposed to the
525 slower adjustment process (24–36 h) in a low Rossby number regime as described in P96.
526 Particularly, the fast process is driven by the mass field as opposed to the momentum field in
527 P96. In concert with the cold air in the lower troposphere and low-level pressure rises, mixing
528 develops that ablates the dust through TKE generation as opposed to the descent of high
529 momentum associated with a tropopause fold for dust ablation in the P96 paradigm. The most
530 unambiguous difference is the irrefutable reliance on mid-to-lower tropospheric cooling in the
531 paradigm shown in Figure 21 as opposed to the occurrence of mid-to-lower tropospheric
532 warming consistent with isentropic sinking motions in P96. The observations and model
533 simulations strongly supported cooling as opposed to warming.

534 **6. Summary and Conclusion**

535 This study is best viewed as a mesoscale complement to the larger scale analyses of P96
536 providing an alternative interpretation of the dynamical processes that organized the widespread
537 turbulence in the Interstate-5 (I-5) dust storm event in the Central Valley of California using a
538 high-resolution Weather Research and Forecasting (WRF) model simulation. An important
539 finding emerges from this study, following the notion of the new paradigm of dust storm
540 generation by *Lewis et al.* [2011] and *Kaplan et al.* [2011], is that the polar jet exit region must
541 be viewed as a rapidly evolving entity oscillating from a dominance of mass versus momentum
542 advection and not as a slowly evolving monolithic/Q-G feature as viewed by *Danielsen* [1974].
543 The re-examination of this case study through WRF simulations clearly contrasted with the

544 findings of P96 in terms of space and time scales of motion and the source regions of surface
545 dust. The dynamical processes on meso- α and meso- β scales of motion associated with the I-5
546 dust storm event similarly followed the sequence of events associated with the dust storms in
547 northwestern Nevada described in *Lewis et al.* [2011] and *Kaplan et al.* [2011].

548 The WRF results indicated that the air parcels reaching the source regions of dust are not
549 associated with long-period Q-G descent linked to tropopause folds. Air parcels within the
550 planetary boundary layer (PBL) are subjected to rapid accelerations over considerably shorter
551 periods in proximity to meso- β scale regions aloft that are characterized by extreme ageostrophy
552 and higher magnitudes of divergence tendencies following the air motion. This causes the
553 creation of a strong unbalanced direct circulation on the right side of the jet's exit region, and the
554 adjustments associated with this mesoscale circulation feature create an environment for dust
555 storm generation. This is achieved through the development of a deep adiabatic layer in the
556 lower troposphere coupled with low-level mass flux convergence that enhances the low-level
557 isallobaric winds close to the source region of surface dust. The dust is in turn ablated by the
558 low-level turbulence.

559 The study clearly indicates that the time scale of adjustments to geostrophic imbalance
560 about the upper-level jet streak is the order of 6 – 12 h. This is in stark contrast to the longer
561 period (24 – 36 h) of adjustment in the Danielsen paradigm. Further, it is adjustment of the mass
562 field that dominates. The following statement from Danielsen makes it clear that momentum
563 adjustment was primary to his view:

564 Isentropic trajectories computed in the jet show that the air decelerates as it
565 descends. On isentropic charts, this deceleration is unambiguous because the wind
566 speeds downstream on the next 12 h map are all slower than they were on the
567 initial map, and the ageostrophic flow itself is usually obvious.

568
569

[*Danielsen* 1974, p218]

570 In short, Danielsen's adjustment focuses on the change in momentum as the descending air
571 parcels encounter weaker pressure gradients. The study of P96 followed the tenets of the
572 Danielsen paradigm [Danielsen 1974] associated with the quasi-geostrophic (Q-G) balanced
573 descent of air accompanying slowly evolving jet streaks linked with tropopause fold. However,
574 the most unambiguous breakdown of this view of the process is highlighted by the fact that the
575 data support substantial and rapid cooling in the upper levels of the PBL. This is in contrast with
576 the Danielsen paradigm that requires longer period warming as isentropes descend rather than
577 being lifted as the evidence supports in this case study.

578 Indeed, the balanced indirect circulation about the jet that is central to the downward
579 angling trajectory on the warm side of the jet in the Danielsen paradigm plays an important role
580 in the upper-level (quasi-geostrophic) frontogenesis. The unbalanced dynamics that drive the
581 dust storm occur in conjunction with upper-level frontogenesis. And although the frontogenetic
582 process appears secondary to the basic dynamics that govern wind generation at lower-levels, its
583 conspicuous presence provides a valuable background signature of the operative mesoscale
584 processes. An essential element to dust storm generation is bifurcation of the frontal pattern in
585 response to the small-scale but intense direct circulation that moves from the cold to the warm
586 side of the jet. It is this rapidly advancing mesoscale frontal zone that gives rise to the lower-
587 tropospheric isallobaric wind (mass adjustment). Further, by following the low-level back
588 trajectories, the movement of the air from east of the Sierra Summit up and over the crest and
589 down into the San Joaquin Valley of California is a crucial component of the process that leads
590 to instability of the PBL in the region of storm development.

591
592
593
594

APPENDIX A

595

596

597 The terms in equation (2) are defined as follows:

$$598 \quad \left(\frac{d}{dt}\right)\delta \equiv \left(\frac{\partial}{\partial t} + \frac{u}{r_e \cos \varphi} \frac{\partial}{\partial \lambda} + \frac{v}{r_e} \frac{\partial}{\partial \varphi} + \omega \frac{\partial}{\partial p}\right)\delta \quad (\text{A1})$$

$$599 \quad \delta = \nabla \cdot \vec{\mathbf{V}}_{\mathbf{H}} = \frac{1}{r_e \cos \varphi} \left[\frac{\partial u}{\partial \lambda} + \frac{\partial}{\partial \varphi} (v \cos \varphi) \right] \quad (\text{A2})$$

$$600 \quad \zeta = \hat{\mathbf{k}} \cdot (\nabla \times \vec{\mathbf{V}}_{\mathbf{H}}) = \frac{1}{r_e \cos \varphi} \left[\frac{\partial v}{\partial \lambda} - \frac{\partial}{\partial \varphi} (u \cos \varphi) \right] \quad (\text{A3})$$

$$601 \quad J(u, v) = \frac{1}{r_e^2 \cos \varphi} \left(\frac{\partial u}{\partial \lambda} \frac{\partial v}{\partial \varphi} - \frac{\partial u}{\partial \varphi} \frac{\partial v}{\partial \lambda} \right) \quad (\text{A4})$$

$$602 \quad \nabla^2 \Phi = \frac{1}{r_e^2} \left[\frac{1}{\cos^2 \varphi} \frac{\partial^2 \Phi}{\partial \lambda^2} + \frac{\partial^2 \Phi}{\partial \varphi^2} \right] - \left(\frac{\tan \varphi}{r_e^2} \right) \frac{\partial \Phi}{\partial \varphi} \quad (\text{A5})$$

$$603 \quad R_{\omega} = -\frac{1}{r_e \cos \varphi} \left[\frac{\partial \omega}{\partial \lambda} \frac{\partial u}{\partial p} + \frac{\partial \omega}{\partial \varphi} \frac{\partial}{\partial p} (v \cos \varphi) \right] \quad (\text{A6})$$

$$604 \quad \beta = \frac{1}{r_e} \frac{\partial f}{\partial \varphi} = \frac{2\Omega \cos \varphi}{r_e} \quad (\text{A7})$$

605

606 where λ and φ are the longitude and latitude, respectively, $\vec{\mathbf{V}}_{\mathbf{H}} (= u\hat{\mathbf{i}} + v\hat{\mathbf{j}})$ is the horizontal

607 velocity vector, u and v are zonal and meridional components of wind, $J(u, v)$ is the Jacobian of

608 the horizontal wind field, and ζ is the vertical component of relative vorticity, ω is the

609 Lagrangian form of vertical velocity, i.e., the rate of change of pressure (p) in a parcel over

610 time, Ω is the angular rotation of the earth, f is the Coriolis parameter ($= 2\Omega \sin \varphi$), β is the

611 latitudinal variation of the Coriolis parameter, Φ is the geopotential, $r_e (= 6371 \text{ km})$ is the

612 radius of the earth, and R_{ω} is the tilting term. Under the assumption of a non-divergent flow,

613 equation (2) degenerates to the non-linear balance equation when the left hand side of equation

614 (2) equals zero [Zhang *et al.* 2002].

615

616

617 **Acknowledgements**

618 Support for this work for John Lewis came from NSSL/NOAA, and support for
619 computational resources came from the Division of Atmospheric Sciences, Desert Research
620 Institute. Additional support for this work came from the Office of Naval Research, program
621 element 0602435N. Data support from the National Climatic Data Center (NCDC) of NOAA is
622 acknowledged. The authors also thank Mr. Travis McCord for providing assistance in making
623 the plots.

624
625
626
627
628
629
630
631
632
633
634
635
636
637
638
639
640
641
642
643
644
645
646
647
648
649
650
651

652 **References**

- 653
654 Barker, E., 1992: Design of the Navy's multivariate optimum interpolation analysis system. *Wea.*
655 *Forecasting*, 7, 220-231.
656
657 Betts, A. K., 1986: A new convective adjustment scheme. Part I: Observational and theoretical
658 basis. *Quart. J. Roy. Met. Soc.*, 111, 1306-1335.
659
660 Betts, A. K., and M. J. Miller, 1986: A new convective adjustment scheme. Part II: Single
661 column tests using GATE WAVE, BOMEX, ATEX and Arctic air-mass data sets. *Quart. J. Roy.*
662 *Met. Soc.*, 112, 693 - 709.
663
664 Bluestein, H. B., 1992: *Synoptic-dynamic meteorology in midlatitudes. I: Principles of*
665 *Kinematics and Dynamics*. Oxford University Press, 448 pp.
666
667 Chen, F., and J. Dudhia, 2001: Coupling an advanced land surface-hydrology model with the
668 Penn State-NCAR MM5 modeling system. Part I: Model implementation and sensitivity. *Mon.*
669 *Wea. Rev.*, 129, 569-585.
670
671 Cram, J.M., M. L. Kaplan, C. A. Mattocks, and J. W. Zack, 1991: The use and analysis of
672 profiler winds to derive mesoscale height and temperature fields: Simulation and real data
673 experiments. *Mon. Wea. Rev.*, 119, 1040-1056.
674
675 Danielsen, E. F., 1968: Stratospheric-tropospheric exchange of radioactivity, ozone, and
676 potential vorticity. *J. Atmos. Sci.*, 25, 502-518.
677
678 Danielsen, E. F., 1974: The relationship between severe weather, major dust storms and rapid
679 large-scale cyclogenesis, Part I. Subsynopticextratropical weather systems: observation, analysis,
680 modeling and prediction. Notes from a Colloquium, Volume II, Seminars and Workshop.
681 National Center for Atmospheric Research, pp. 215-241.
682
683 Dudhia, J., 1989: Numerical study of convection observed during the Winter Monsoon
684 Experiment using a mesoscale two-dimensional model. *J. Atmos. Sci.*, 46, 3363-3391.
685
686 Ek, M.B., K. E. Mitchell, Y. Lin, E. Rogers, P. Grumann, V. Koren, G. Gayno, and J. D.
687 Tarpley, 2003: Implementation of Noah land surface model advances in the National Centers for
688 Environmental Prediction operational mesoscale Eta model. *J. Geophys. Res.*, 108 (D22), 8851.
689
690 Hamilton, D. W., Y.-L. Lin, R. P. Weglarz, and M. L. Kaplan, 1998: Antecedent Jetlet
691 Formation Prior to the Palm Sunday 1994 Tornado Outbreak in Alabama and Georgia. *Mon.*
692 *Wea. Rev.*, 126, 2061-2089.
693
694 Hodur, R.M., 1987: Evaluation of a regional model with an update cycle. *Mon. Wea. Rev.*, 115,
695 2707-2718.
696

697 Janjić, Z. I., 1994: The step-mountain Eta coordinate model: Further developments of the
698 convection, viscous sublayer, and turbulence closure schemes. *Mon. Wea. Rev.*, *122*, 927-945.
699

700 Janjić, Z. I., 1996: The surface layer in the NCEP Eta model. Preprints, 11th Conf. on Numerical
701 Weather Prediction, Norfolk, VA, Amer. Meteor. Soc., 354-355.
702

703 Janjić, Z. I., 2001: Nonsingular Implementation of the Mellor–Yamada Level 2.5 Scheme in the
704 NCEP Meso Model, NCEP Office Note, No. 437, 61 pp.
705

706 Kaplan, M. L., S. E. Koch, Y.-L. Lin, R. P. Weglarz, and R. A. Rozumalski, 1997: Numerical
707 simulations of a gravity wave event over CCOPE. Part I: The role of geostrophic adjustment in
708 mesoscale jetlet formation. *Mon. Wea. Rev.*, *125*, 1185-1211.
709

710 Kaplan, M. L., Y.-L. Lin, D. W. Hamilton, and R. A. Rozumalski, 1998: A numerical simulation
711 of an unbalanced jetlet and its role in the Palm Sunday 1994 tornado outbreak in Alabama and
712 Georgia. *Mon. Wea. Rev.*, *126*, 2133-2165.
713

714 Kaplan, M. L., R. K. Vellore, J. M. Lewis, and M. Young, 2011: The role of unbalanced
715 mesoscale circulations in dust storms. *J. Geophys. Res.*, In Print.
716

717 Karyampudi, V. M., M. L. Kaplan, S. E. Koch, and R. Zamora, 1995a: The Influence of the
718 Rocky Mountains in the 13-14 April 1986 severe weather outbreak. Part I: Mesoscale lee
719 cyclogenesis and its relationship to severe weather and dust storms. *Mon. Wea. Rev.*, *123*, 1394 -
720 1422.
721

722 Karyampudi, V. M., Koch, S. E., C. Chen, J. W. Rottman, and M. L. Kaplan, 1995b: The
723 influence of the Rocky Mountains in the 13-14 April 1986 severe weather outbreak. Part II:
724 Evolution of a pre-frontal bore and its role in triggering a squall line. *Mon. Wea. Rev.*, *123*, 1423
725 - 1446.
726

727 Koch, S. E., and P. B. Dorian, 1988: A mesoscale gravity wave event observed during CCOPE.
728 Part III: Wave environment and probable source mechanisms. *Mon. Wea. Rev.*, *116*, 2570-2592.
729

730 Lewis, J. M., M. L. Kaplan, R. Vellore, R. M. Rabin, J. Hallett, and S. Cohn, 2011: Dust storm
731 over the Black Rock Desert: Large-scale dynamic signatures. *J. Geophys. Res.*, *116*, D06113,
732 doi: 10.1029/2010JD014784.
733

734 Liou, C.-S., R. M. Hodur, and R. H. Langland, 1994: Navy Operational Atmospheric Prediction
735 System (NORAPS): A triple nested mesoscale model. Preprints, *10th Conf. on Numerical
736 Weather Prediction*, Portland, OR, Amer. Meteor. Soc., 423–425.
737

738 Martin, J. E., 2006: *Mid-latitude Atmospheric Dynamics: A First Course*. John Wiley & Sons,
739 363pp.
740

741 Mellor, G. L., and T. Yamada, 1974: A hierarchy of turbulence closure models for planetary
742 boundary layers. *J. Atmos. Sci.*, *31*, 1791-1806.

743 Mellor, G. L., and T. Yamada, 1982: Development of a turbulence closure model for geophysical
744 fluid problems. *Rev. Geophys. Space Phys.*, *20*, 851-875.
745

746 Mesinger F., and Coauthors, 2006: North American Regional Reanalysis. *Bull. Amer. Meteor.*
747 *Soc.*, *87*, 343–360.
748

749 Mlawer, E. J., S. J. Taubman, P. D. Brown, M. J. Iacono, and S. A. Clough, 1997: Radiative
750 transfer for inhomogeneous atmosphere: RRTM, a validated correlated-k model for the
751 longwave. *J. Geophys. Res.*, *102 (D14)*, 16663–16682.
752

753 O' Sullivan, D., and T. J. Dunkerton, 1995: Generation of inertia-gravity waves in a simulated
754 life cycle of baroclinic instability. *J. Atmos. Sci.*, *52*, 3695-3716.
755

756 Pauley, P. M., N. L. Baker and E. H. Barker, 1996: An observational study of the “Interstate 5”
757 dust storm case study. *Bull. Amer. Meteor. Soc.*, *77*, 693-720.
758

759 Rochette, S.M., and P. S. Market, 2006: A primer on the ageostrophic wind. *Natl. Wea. Dig.*, *30*,
760 17-28.
761

762 Skamarock, W. C., and Coauthors, 2008: *A Description of the Advanced Research WRF Version*
763 *3.NCAR/TN-475+STR*, 113 pp.
764

765 Thompson, G., R. M. Rasmussen, and K. Manning, 2004: Explicit forecasts of winter
766 precipitation using an improved bulk microphysics scheme. I: Description of sensitivity analysis.
767 *Mon. Wea. Rev.*, *132*, 519-542.
768

769 Thompson, G., P. R. Field, W. D. Hall, and R. M. Rasmussen, 2006: A new bulk microphysics
770 parameterization for WRF and MM5. Seventh Weather and Research Forecasting Workshop,
771 National Center for Atmospheric Research, Boulder, CO, NCAR.
772

773 Uccellini, L. W., and D. R. Johnson, 1979: The coupling of upper and lower tropospheric jet
774 streaks and implications for the development of severe convective storms. *Mon. Wea. Rev.*, *107*,
775 682-703.
776

777 Van Tuyl, A. H., and J. A. Young, 1982: Numerical simulation of nonlinear jet stream
778 adjustment. *Mon. Wea. Rev.*, *110*, 2038-2054.
779

780 Zack, J. W., and M. L. Kaplan, 1987: Numerical simulations of the subsynoptic features
781 associated with the AVE-SESAME I Case, Part I: The pre-convective environment. *Mon. Wea.*
782 *Rev.*, *115*, 2367-2394.
783

784 Zhang, F., S. E. Koch, C. A. Davis, and M. L. Kaplan, 2002: A survey of unbalanced flow
785 diagnostics and their applications. *Adv. Atmos. Sci.*, *17*, 165-183.
786
787
788

789 **TABLE CAPTIONS**

790
791 Table 1. Locations of the surface and upper-air* stations, their locations and elevations from
792 mean sea level referenced in the study (see also Figures 1 and 2 for the geographical locations).

793
794 Table 2. Observed wind speed maximum (m s^{-1}), wind gust maximum (m s^{-1}), and the lowest
795 visibility (km) recorded during 1100-2300 UTC 29 November 1991 at stations in Nevada (NV)
796 and California (CA) (Source: <http://www.ncdc.noaa.gov>) (see Table 1 and Figure 2 for the
797 geographical locations of the stations; cf Table 1 of *Pauley et al.* [1996] for more details).

798
799 Table 3. 18 km WRF diagnosed time series of the terms ($\times 10^{-8} \text{ s}^{-2}$) in Equation (2) at 500 hPa
800 valid from 1200 UTC 29 November 1991 (11/29) to 0000 UTC 30 November 1991 (11/30).
801 Location is 37° N , 120.4° W . Also shown is the column-integrated mass flux divergence ($\times 10^{-3}$
802 $\text{kg m}^{-2} \text{ s}^{-1}$) at this location [z_T = height at the model top; ρ = air density; \vec{V} = velocity vector].

803
804
805
806
807
808
809
810
811
812
813
814
815
816
817
818
819
820
821
822
823
824
825
826
827
828
829
830
831
832
833
834

835
836
837
838
839
840
841
842
843
844

Table 1. Locations of the surface and upper-air* stations, their locations and elevations from mean sea level referenced in the study (see also Figures 1 and 2 for the geographical locations).

Station name (in alphabetical order), U.S. State	Station Identifier	Latitude (°N)	Longitude (°W)	Elevation MSL (m)
Bakersfield, CA	BFL	35.43	119.06	155
Bishop, CA	BIH	37.37	118.36	1256
*Boise, ID	BOI	43.56	116.22	875
Coalinga, CA	COA	36.14	120.36	205
Edwards AFB, CA	EDW	34.92	117.87	704
*Elko, NV	LKN	40.82	115.79	1567
Fallon, NV	NFL	39.42	118.70	1199
Fresno, CA	FAT	36.78	119.72	102
Lemoore, CA	NLC	36.33	119.95	71
Los Angeles, CA	LAX	33.94	118.41	38
Lovelock, NV	LOL	40.07	118.57	1190
Merced, CA	MCE	37.28	120.51	48
Modesto, CA	MOD	37.63	120.95	30
*Oakland, CA	OAK	37.72	122.22	3
Paso Robles, CA	PRB	35.67	120.63	255
Redding, CA	RDD	40.51	122.29	154
*Reno, NV	REV	39.50	119.77	1346
Sacramento, CA	SAC	38.51	121.49	7
*Salem, OR	SLE	44.91	123.00	65
Salinas, CA	SNS	36.66	121.61	26
*San Diego, CA	NKX	32.85	117.11	128
South Lake Tahoe, CA	TVL	38.90	120.00	1909
Spokane, WA	OTX	47.68	117.62	729
Truckee, CA	TRK	39.32	120.14	1798
*Vandenberg, CA	VBG	34.74	120.58	112
Winnemucca, NV	WMC	40.90	117.81	1313

845
846
847
848

849
 850
 851
 852
 853
 854
 855
 856
 857
 858
 859
 860
 861
 862
 863

Table 2. Observed wind speed maximum (m s^{-1}), wind gust maximum (m s^{-1}), and the lowest visibility (km) recorded during 1100-2300 UTC 29 November 1991 at stations in Nevada (NV) and California (CA) (Source: <http://www.ncdc.noaa.gov>) (see Table 1 and Figure 2 for the geographical locations of the stations; cf Table 1 of Pauley *et al.* [1996] for more details).

Stations	Maximum wind speed (m s^{-1})/wind direction during 1100–2300 UTC 29 November 1991	Maximum gust speed (m s^{-1})	Lowest visibility (km)
WMC	13.4/320°	18.4	4.8 (1130 UTC)
LOL	11.2/340°	16.1	0.8 (1300 UTC)
NFL	10.3/360°	17.0	0.8 (1500 UTC)
REV	10.4/20°	13.0	16.2 (2000 UTC)
TVL	6.2/350°	13.0	9.6 (2130 UTC)
TRK	13.4/30°	18.0	6.4 (1800 UTC)
MCE	10.3/340°	14.3	6.4 (2100 UTC)
MOD	11.2/330°	16.6	16.1 (2100 UTC)
PRB	17.0/320°	21.5	0.8 (2100 UTC)
BFL	13.4/330°	16.6	3.2 (2230 UTC)
NLC	15.7/330°	21.5	0.6 (2300 UTC)

864
 865
 866
 867
 868
 869

Table 3. 18 km WRF diagnosed time series of the terms ($\times 10^{-8} \text{ s}^{-2}$) in Equation (2) at 500 hPa valid from 1200 UTC 29 November 1991 (11/29) to 0000 UTC 30 November 1991 (11/30). Location is 37° N , 120.4° W . Also shown is the column-integrated mass flux divergence ($\times 10^{-3} \text{ kg m}^{-2} \text{ s}^{-1}$) at this location [z_T = height at the model top; ρ = air density; \vec{V} = velocity vector].

Time (MM/DD)	$\frac{d\delta}{dt}$ ($\times 10^{-8}$)	R_ω ($\times 10^{-8}$)	$f\zeta - u\beta$ ($\times 10^{-8}$)	$2J(u, v)$ ($\times 10^{-8}$)	$-\nabla^2\Phi$ ($\times 10^{-8}$)	$\int_{z=0}^{z=z_T} [\nabla \cdot (\rho \vec{V})] dz$ ($\times 10^{-3} \text{ kg m}^{-2} \text{ s}^{-1}$)
1200 UTC (11/29)	0.27	0.58	-0.07	-0.03	-0.13	-1.7
1300 UTC (11/29)	-0.73	1.35	0.03	0.19	-2.21	-1.9
1400 UTC (11/29)	-3.93	0.78	0.10	1.03	-5.83	-1.4
1500 UTC (11/29)	1.12	0.93	-0.00	0.92	-0.67	+2.3
1600 UTC (11/29)	0.74	1.52	-0.26	-0.36	0.14	-1.1
1700 UTC (11/29)	-0.66	0.13	-0.57	-0.96	0.81	-3.1
1800 UTC (11/29)	2.45	-0.12	-0.68	0.06	3.28	+1.4
1900 UTC (11/29)	5.10	0.09	-0.64	1.89	4.20	+0.8
2000 UTC (11/29)	4.11	1.08	-0.44	3.54	0.54	+1.1
2100 UTC (11/29)	-1.60	-0.11	-0.36	4.50	-5.48	+1.9
2200 UTC (11/29)	-2.85	-0.36	-0.29	5.08	-7.20	+0.8
2300 UTC (11/29)	-7.75	0.89	-0.12	3.83	-12.31	-2.8
0000 UTC (11/30)	0.65	0.60	-0.00	1.98	-1.83	-3.4

FIGURE CAPTIONS

Figure 1. WRF modeling domains and horizontal grid dimensions in x - and y - directions, respectively: 157×127 grid points (54 km grid), 247×247 grid points (18 km grid), 451×451 grid points (6 km grid), and 721×721 grid points (2 km grid). [WA=Washington, OR=Oregon, ID=Idaho, NV=Nevada, CA=California, UT=Utah, AZ=Arizona, CO=Colorado, and NM=New Mexico].

Figure 2. Representation of topography (shaded) in California and Nevada in the innermost modeling domain (Source: U.S. Geological Survey). Overlaid are the cross sections J-J', K-K', and L-L' and station identifiers referenced in the study. An asterisk is shown at the location where multiple accidents are reported on I-5 in the San Joaquin Valley of California.

Figure 3. NARR analyses of 500 hPa geopotential height (solid; contour interval = 60 m), wind speed (shaded; m s^{-1}), and air temperature (dashed; contour interval = 2 °C) at 1200 UTC 29 November 1991.

Figure 4. Tropopause pressure (hPa) diagnosed from NARR at (a) 0600 UTC and (b) 1800 UTC 29 November 1991.

Figure 5. WRF (2 km grid) simulated 500 hPa temperature (dashed; contour interval = 2° C) and geopotential height (solid; contour interval = 60 m) and horizontal wind speeds (shaded; m s^{-1}) valid at 1500 UTC 29 November 1991. Overlain are the simulated horizontal winds (full barb = 5 m s^{-1} ; plotted at every 60 km interval) at 800 hPa.

Figure 6. Same as described in Figure 5, but valid for 2100 UTC 29 November 1991.

Figure 7. Planview of Lagrangian backtrajectory diagnosed from 18 km WRF grid starting at 2300 UTC 29 November 1991 above Fresno (FAT), California (COA) from the pressure level 900 hPa. The width of the arrows indicates the rising and sinking of the parcel motion. Locations of the stations BOI, OTX, LKN, SLE, REV, MCE, and BIH (see also Table 1) are indicated in the figure.

Figure 8. Diagnostics for wind speed (m s^{-1}), ageostrophic wind speed (m s^{-1}), parcel acceleration ($\times 10^3 \text{ m s}^{-2}$), air temperature (°C), sea level pressure (hPa), mixing layer depth (m), sensible heat flux at the surface (W m^{-2}), TKE (J kg^{-1}), and Richardson number (dimensionless) along the backtrajectory. Terrain height (km) along the parcel trajectory, pressure (hPa) and the corresponding height (km) ASL at which the parcel is located are also shown in the figure. The starting time (pressure level) of the trajectory is 2300 UTC 29 November 1991 (900 hPa) above FAT. Time (UTC) on 29 November 1991 is shown on the x-axis.

Figure 9. 18-km WRF diagnosed total wind shear (light; full barb = 5 m s^{-1}) and geostrophic wind shear (dark) in the 500 – 700 hPa layer valid at (a) 1200, (b) 1400, (c) 1600 and (d) 1800 UTC 29 November 1991.

Figure 10. Ageostrophic wind vectors at 500 hPa diagnosed from 6-km WRF forecasts at 1200, 1500, 1800 and 2100 UTC 29 November 1991.

Figure 11. 2-km WRF diagnosed Lagrangian Rossby number (Ro^L) at 500 hPa valid for (a) 1500 and (b) 1800 UTC 29 November 1991. Locations of the stations REV, SAC, MOD, MCE, FAT, COA, BFL (see Table 1) are shown on the figure.

Figure 12. 18 km WRF simulated potential temperature (dashed; contour interval = 2 K), horizontal winds (full barb = 5 m s⁻¹), wind speeds (solid; contour interval = 5 m s⁻¹), vertical p-velocity (ω) (shaded; red = upward; blue = downward; $\mu\text{b s}^{-1}$) at 1500 UTC 29 November 1991 along the cross section J-J' shown in Figure 2. Magnitudes of vertical motion are indicated inside the arrows. Overlain in the figures are the total wind jet maximum (J) and locations of OAK and NFL along the cross section.

Figure 13. 18 km WRF simulated wind speeds (solid; contour interval = 5 m s⁻¹), diagnosed quasi-geostrophic vertical p-velocity (QG- ω) (shaded; red = upward; blue = downward; $\mu\text{b s}^{-1}$) at 1500 UTC 29 November 1991 along the cross section J-J' shown in Figure 2. Magnitudes of vertical motion are indicated inside the arrows. Overlain in the figures are the total wind jet maximum (J), geostrophic wind jet maximum (J_g) and locations of OAK and NFL along the cross section.

Figure 14. Same as described in Figure 12, but along the cross section K-K' (see Figure 2 for the orientation of the cross section) valid at 1800 UTC 29 November 1991.

Figure 15. Same as described in Figure 13, but along the cross section K-K' (see Figure 2 for the orientation of the cross section) valid at 1800 UTC 29 November 1991.

Figure 16. 2-km WRF diagnosed mean temperature (contour interval = 2°C) in the 500 – 700 hPa layer valid at 1200, 1400, 1600 and 1800 UTC 29 November 1991.

Figure 17. 2-km WRF simulated profiles of air temperature (°C) and horizontal winds (full barb = 5 m s⁻¹) at Lemoore (NLC) and Bakersfield (BFL), California valid at (a,c) 1800 UTC 29 November 1991, and (b,d) 0000 UTC 30 November 1991.

Figure 18. 6 km WRF diagnosed isallobaric winds (normalized vector lengths) from the 3-h mean sea level pressure tendency [contour interval = 1 mb] during (a) 1500–1800 UTC and (b) 1800-2100 UTC 29 November 1991. Locations of SAC, MCE, FAT, BIH, COA, BFL, and REV are shown in the figure.

Figure 19. 6 km WRF simulated TKE (shaded; J kg⁻¹), horizontal winds (full barb = 5 m s⁻¹), potential temperature (solid; contour interval = 2.5 K) along the cross section L-L' (shown in Figure 2) at 1800 UTC 29 November 1991. Nearest locations to Reno (REV) and Coalinga (COA) are shown on the figure.

Figure 20. Same as described in Figure 18, but valid at 2200 UTC 29 November 1991.

Figure 21. Schematic of the unbalanced circulations and fast adjustment signals during 1500 UTC 29 November 1991 – 0000 UTC 30 November 1991.

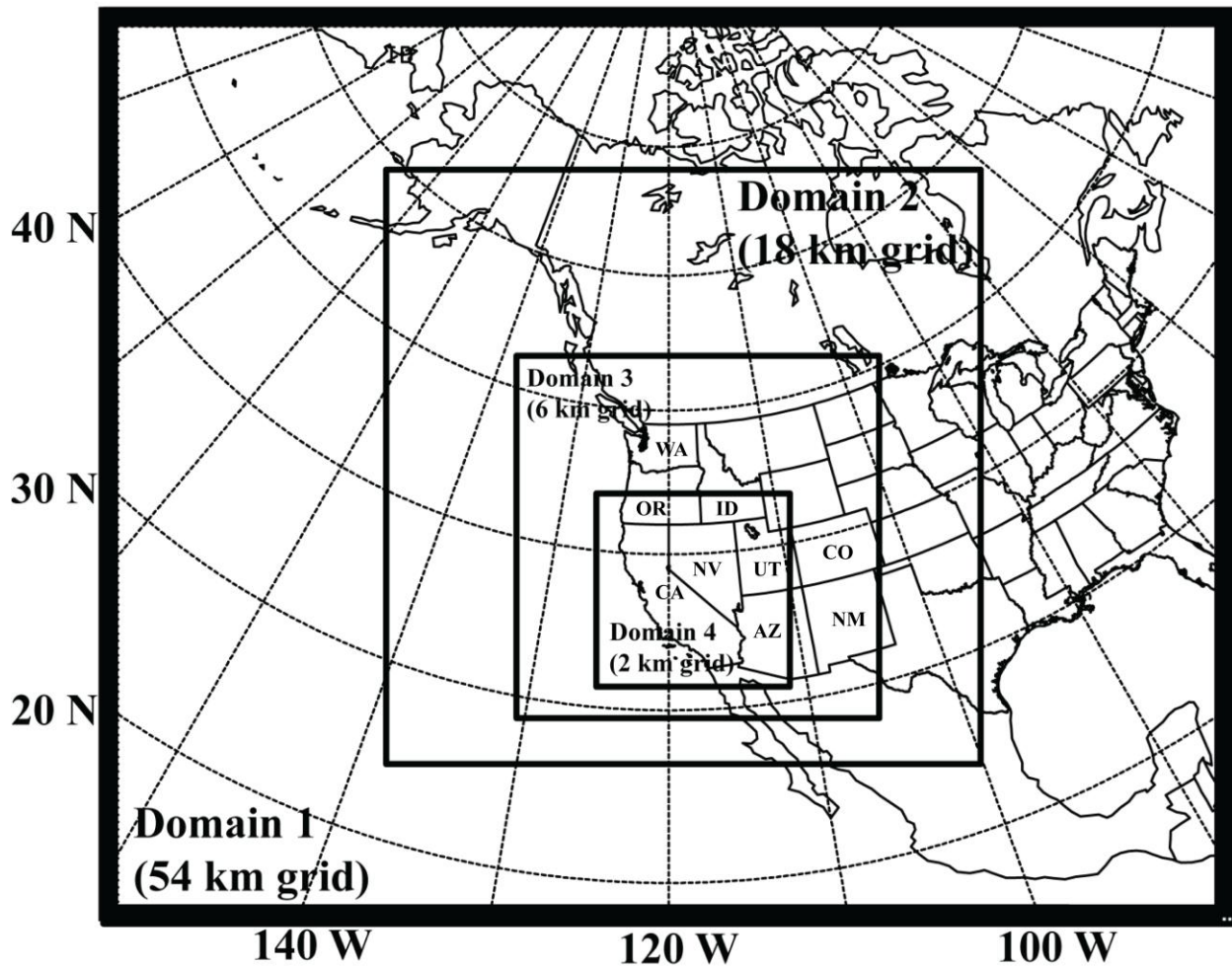


Figure 1. WRF modeling domains and horizontal grid dimensions in x - and y - directions, respectively: 157×127 grid points (54 km grid), 247×247 grid points (18 km grid), 451×451 grid points (6 km grid), and 721×721 grid points (2 km grid). [WA=Washington, OR=Oregon, ID=Idaho, NV=Nevada, CA=California, UT=Utah, AZ=Arizona, CO=Colorado, and NM=New Mexico].

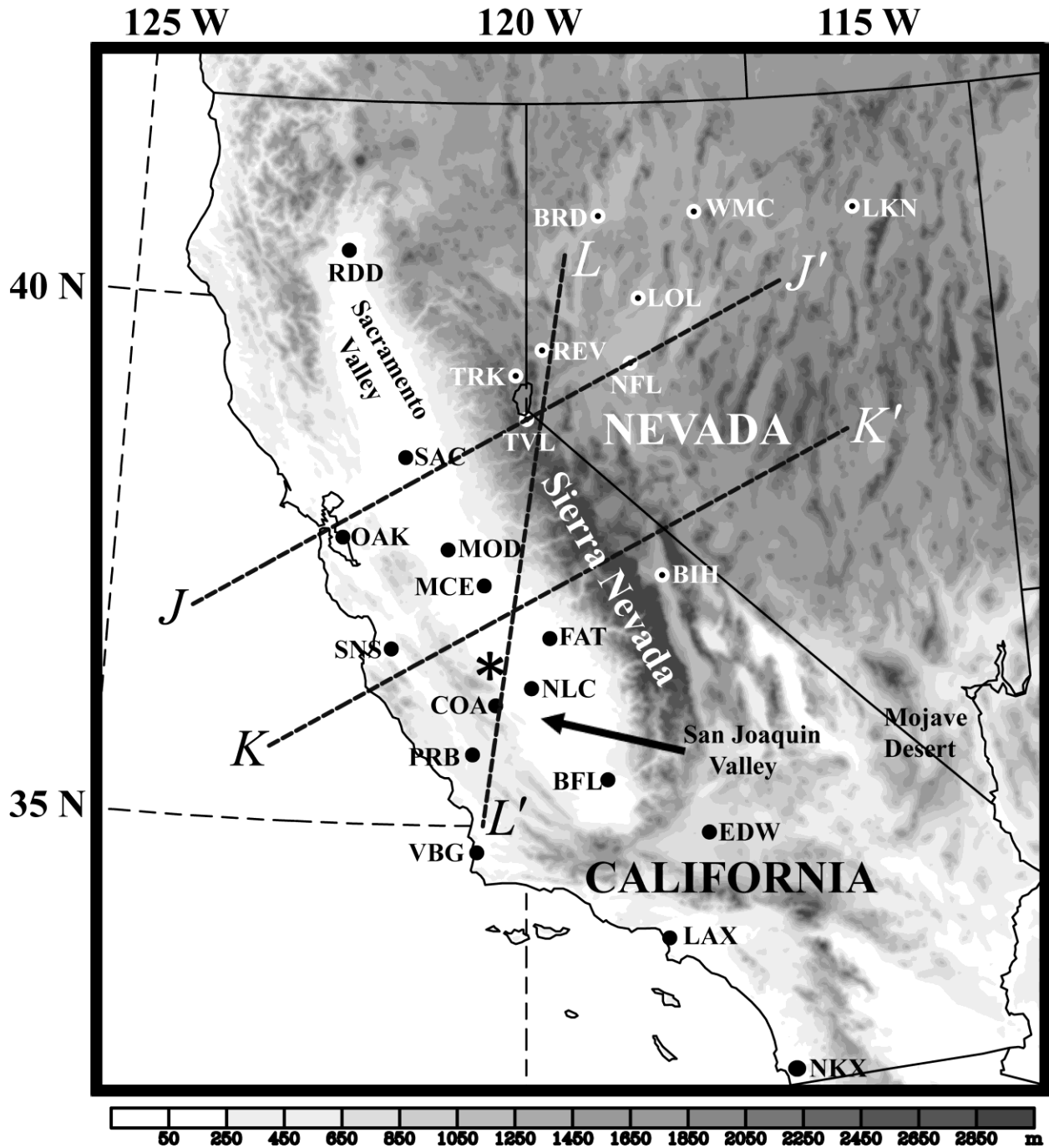


Figure 2. Representation of topography (shaded) in California and Nevada in the innermost modeling domain (Source: U.S. Geological Survey). Overlaid are the cross sections J-J', K-K', and L-L', and station identifiers referenced in the study. An asterisk is shown at the location where multiple accidents are reported on I-5 in the San Joaquin Valley of California.

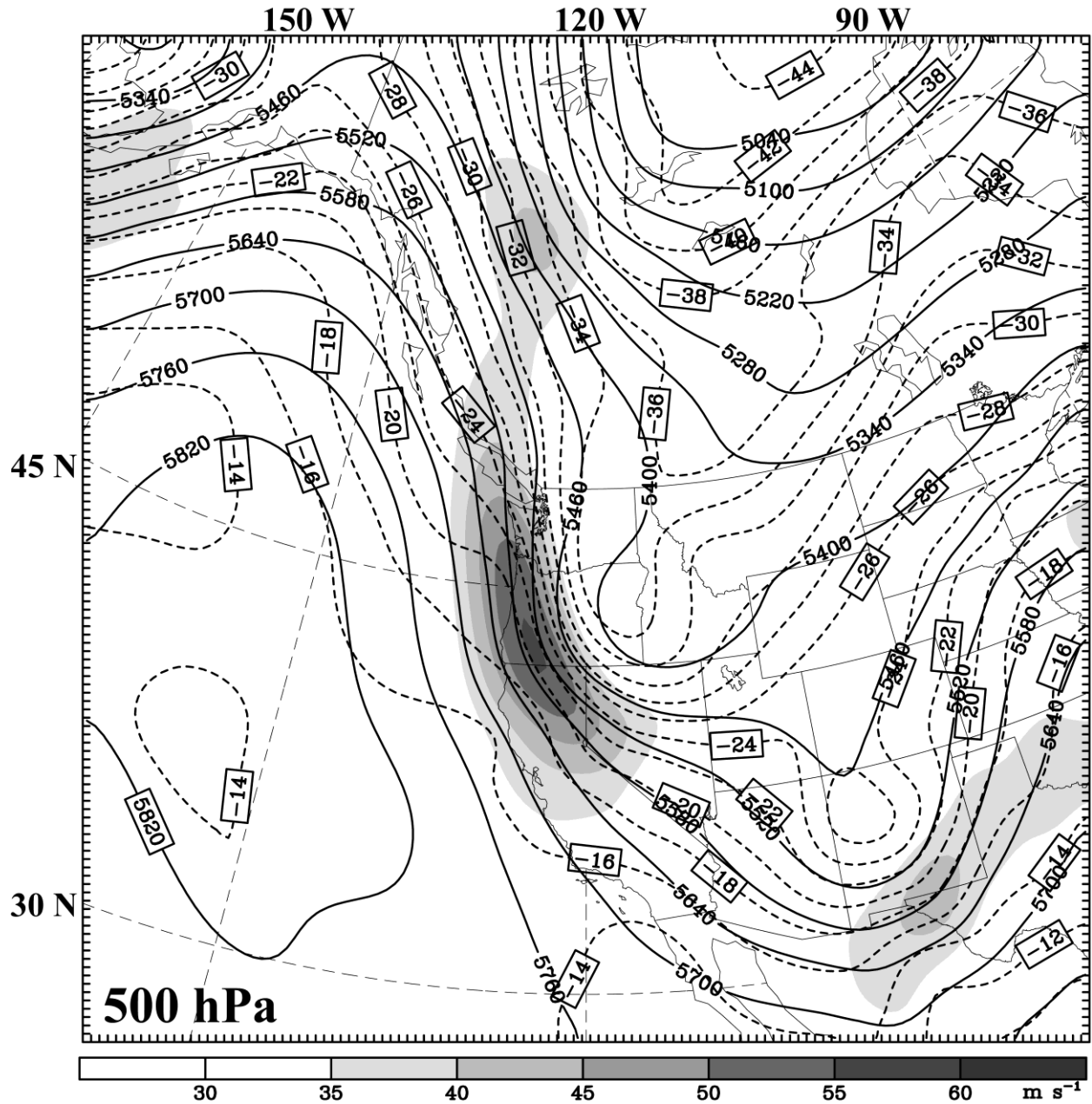


Figure 3. NARR analyses of 500 hPa geopotential height (solid; contour interval = 60 m), wind speed (shaded; m s⁻¹), and air temperature (dashed; contour interval = 2 °C) valid at 1200 UTC 29 November 1991.

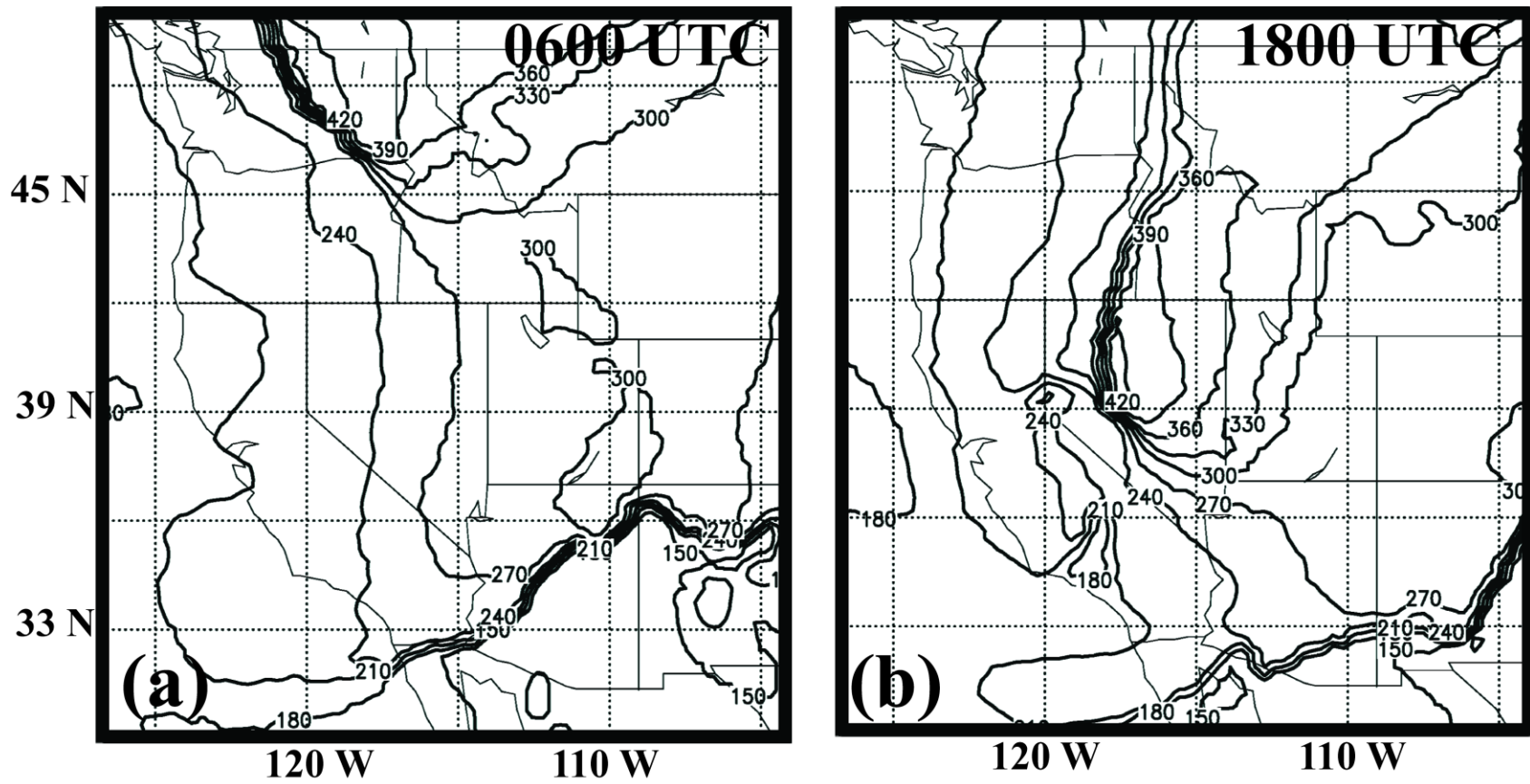


Figure 4. Tropopause pressure (hPa) diagnosed from NARR at (a) 0600 UTC and (b) 1800 UTC 29 November 1991.

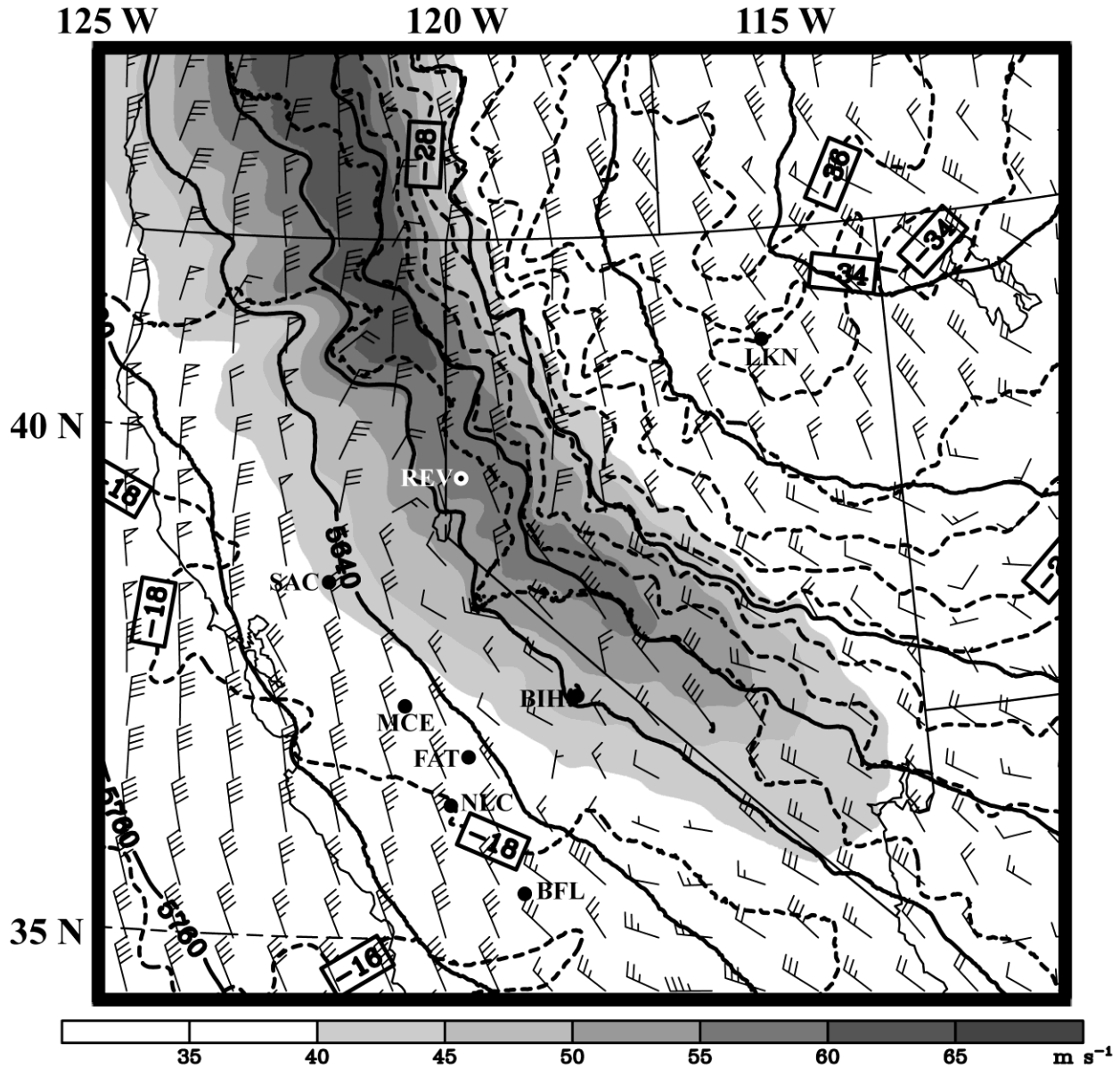


Figure 5. WRF (2 km grid) simulated 500 hPa temperature (dashed; contour interval = 2° C) and geopotential height (solid; contour interval = 60 m) and horizontal wind speeds (shaded; m s⁻¹) valid at 1500 UTC 29 November 1991. Overlain are the simulated horizontal winds (full barb = 5 m s⁻¹; plotted at every 60 km interval) at 800 hPa.

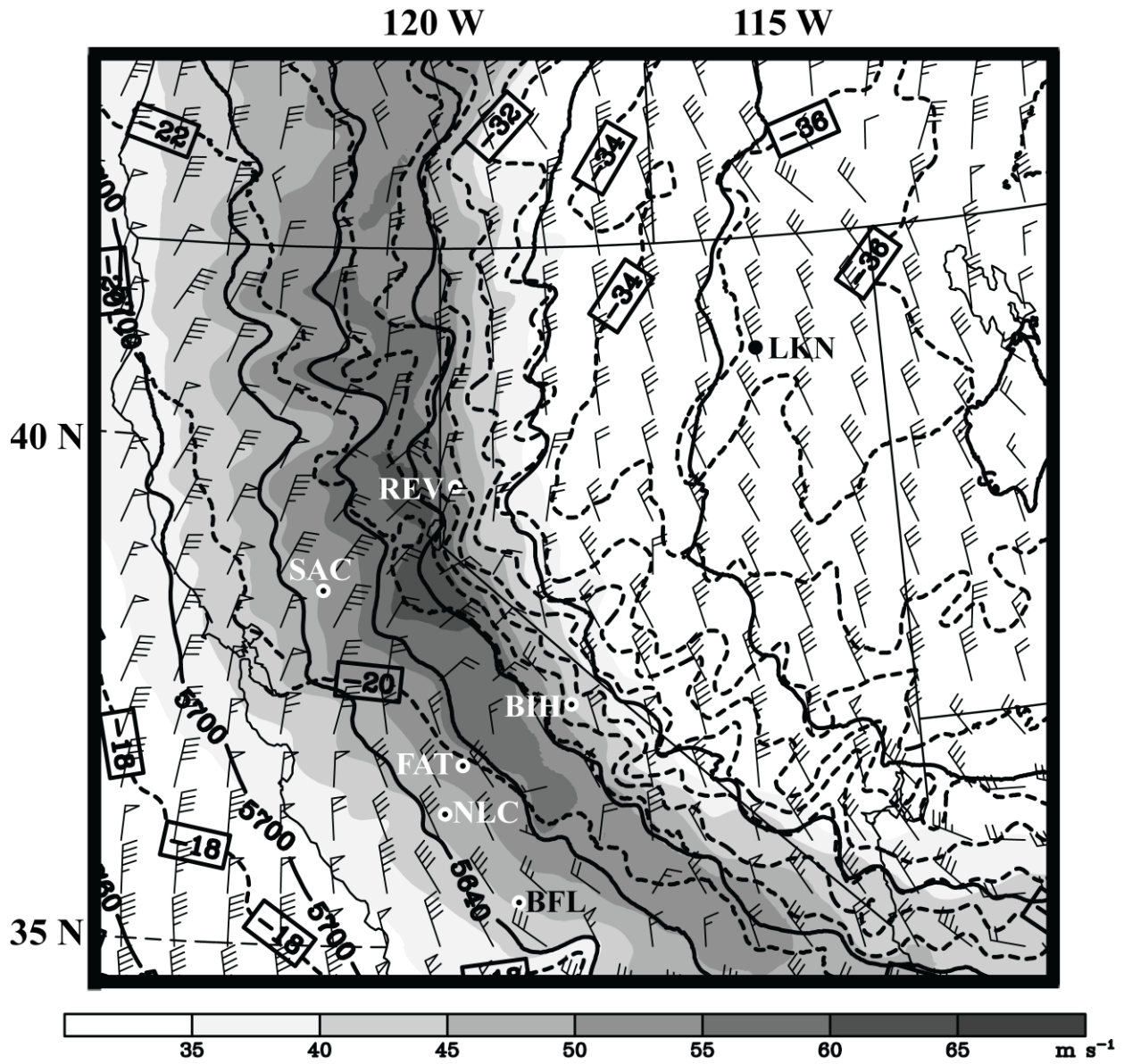


Figure 6. Same as described in Figure 5, but valid for 2100 UTC 29 November 1991.

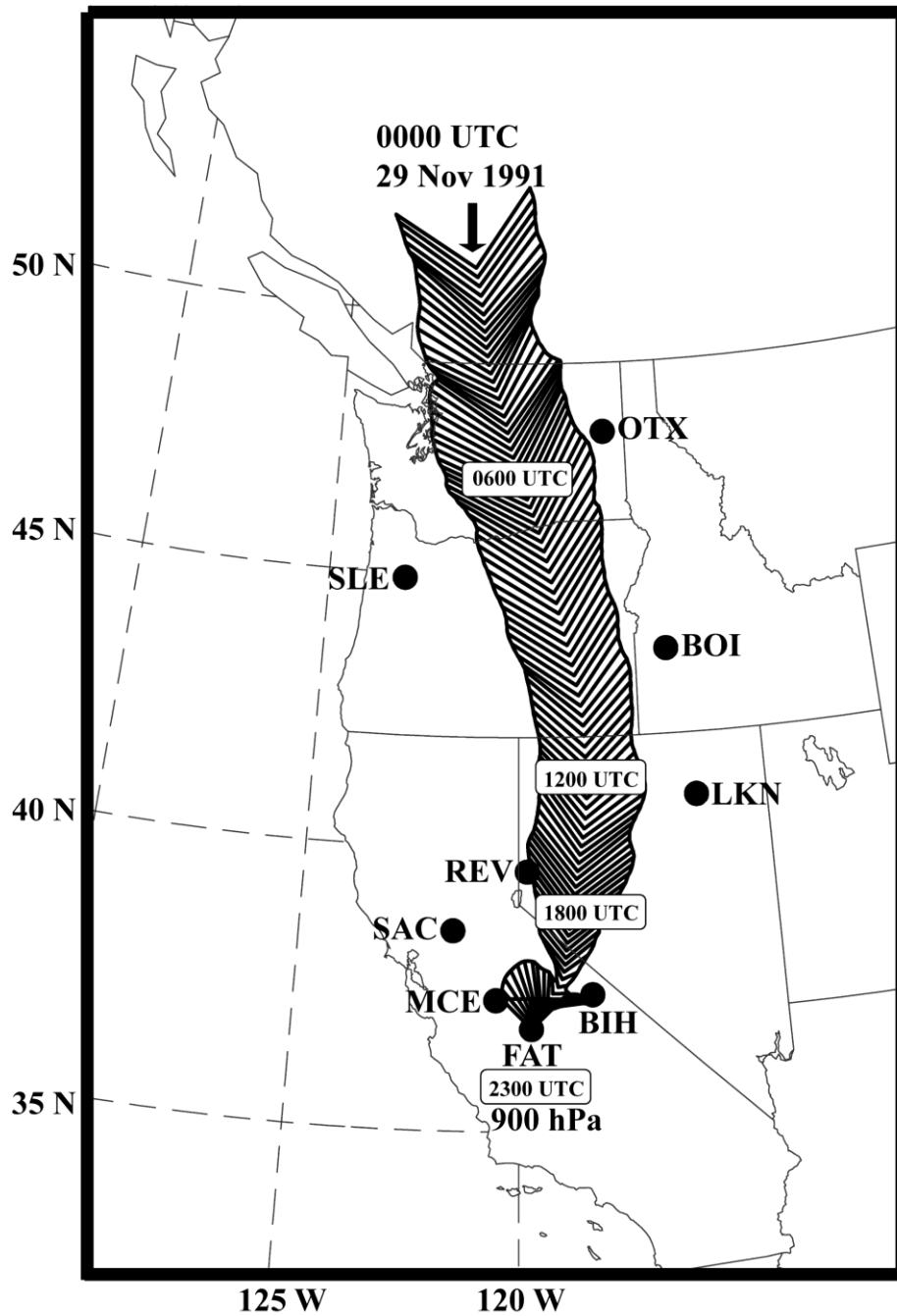


Figure 7. Planview of Lagrangian backtrajectory diagnosed from 18 km WRF grid starting at 2300 UTC 29 November 1991 above Fresno (FAT), California from the pressure level 900 hPa. The width of the arrows indicates the rising and sinking of the parcel motion. Locations of the stations BOI, OTX, LKN, SLE, REV, MCE, and BIH (see also Table 1) are indicated in the figure.

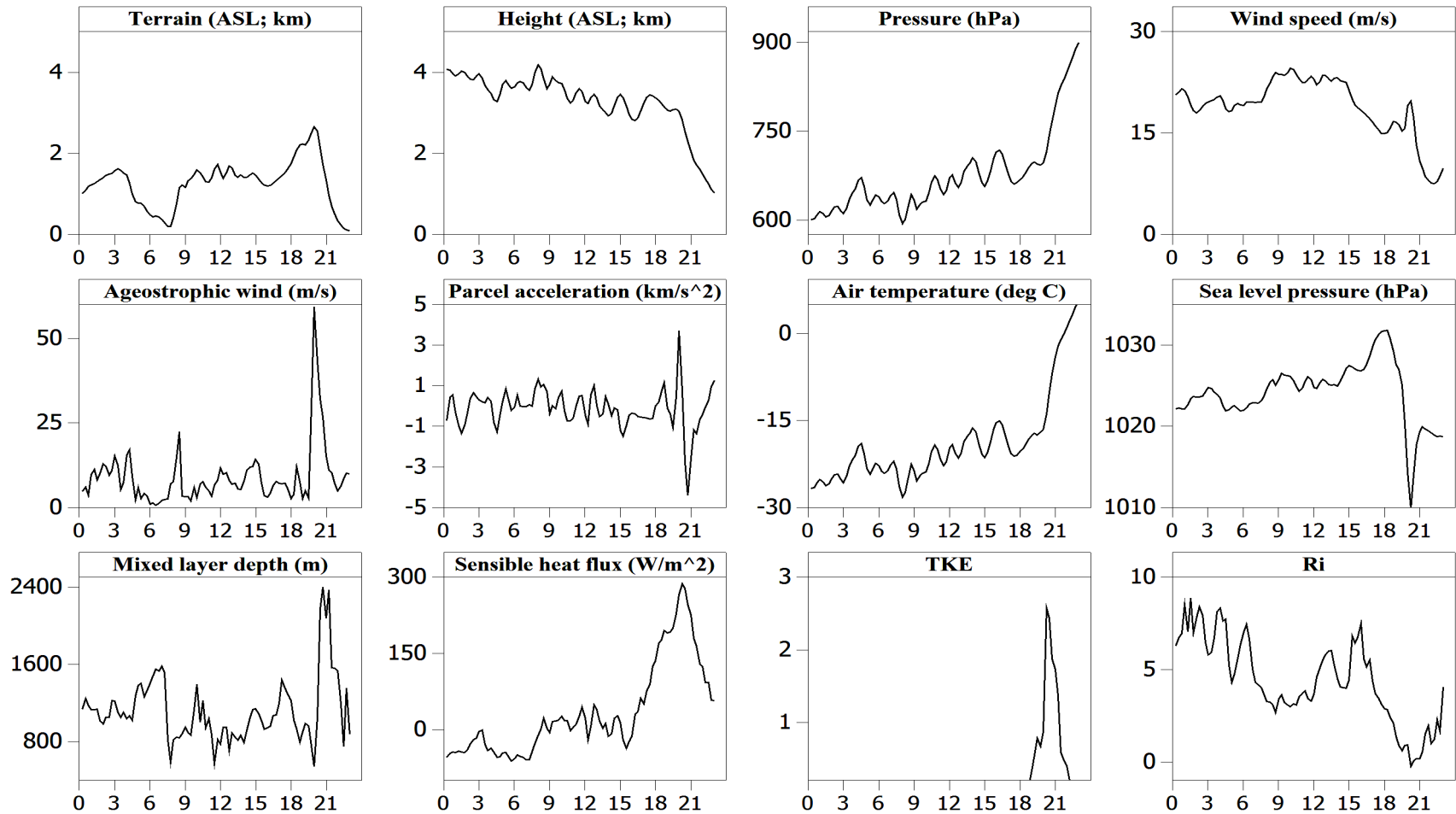


Figure 8. Diagnostics for wind speed (m s^{-1}), ageostrophic wind speed (m s^{-1}), parcel acceleration ($\times 10^3 \text{ m s}^{-2}$), air temperature ($^{\circ}\text{C}$), sea level pressure (hPa), mixing layer depth (m), sensible heat flux at the surface (W m^{-2}), TKE (J kg^{-1}), and Richardson number (dimensionless) along the backtrajectory. Terrain height (km), pressure (hPa) and the corresponding height (km) ASL along the parcel trajectory are also shown in the figure. The starting time (pressure level) of the trajectory is 2300 UTC 29 November 1991 (900 hPa) above Fresno, CA (FAT). Time (UTC) on 29 November 1991 is shown on the x-axis.

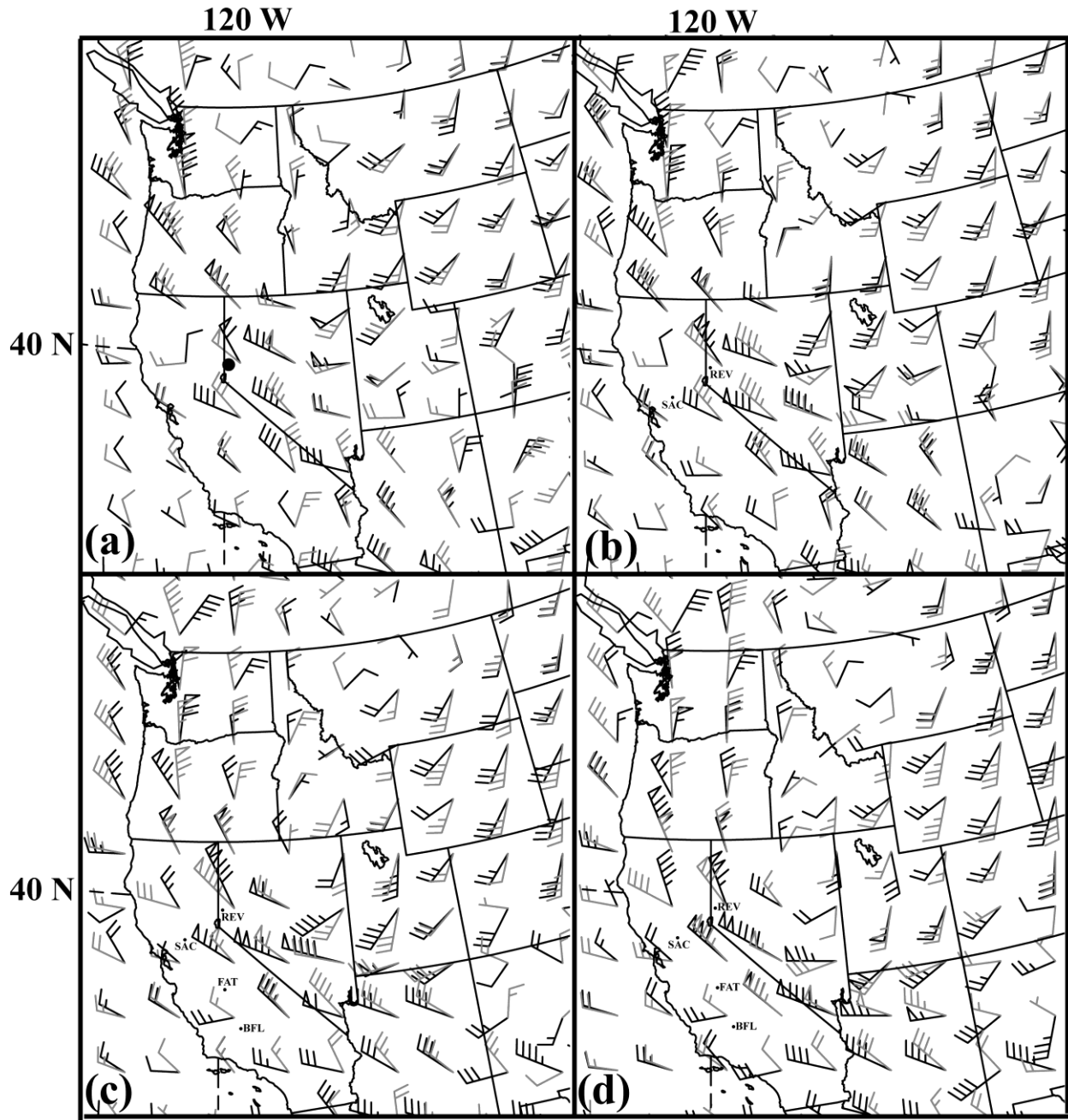


Figure 9. 18-km WRF diagnosed total wind shear (light; full barb = 5 m s^{-1}) and geostrophic wind shear (dark) in the 500 – 700 hPa layer valid at (a) 1200, (b) 1400, (c) 1600 and (d) 1800 UTC 29 November 1991.

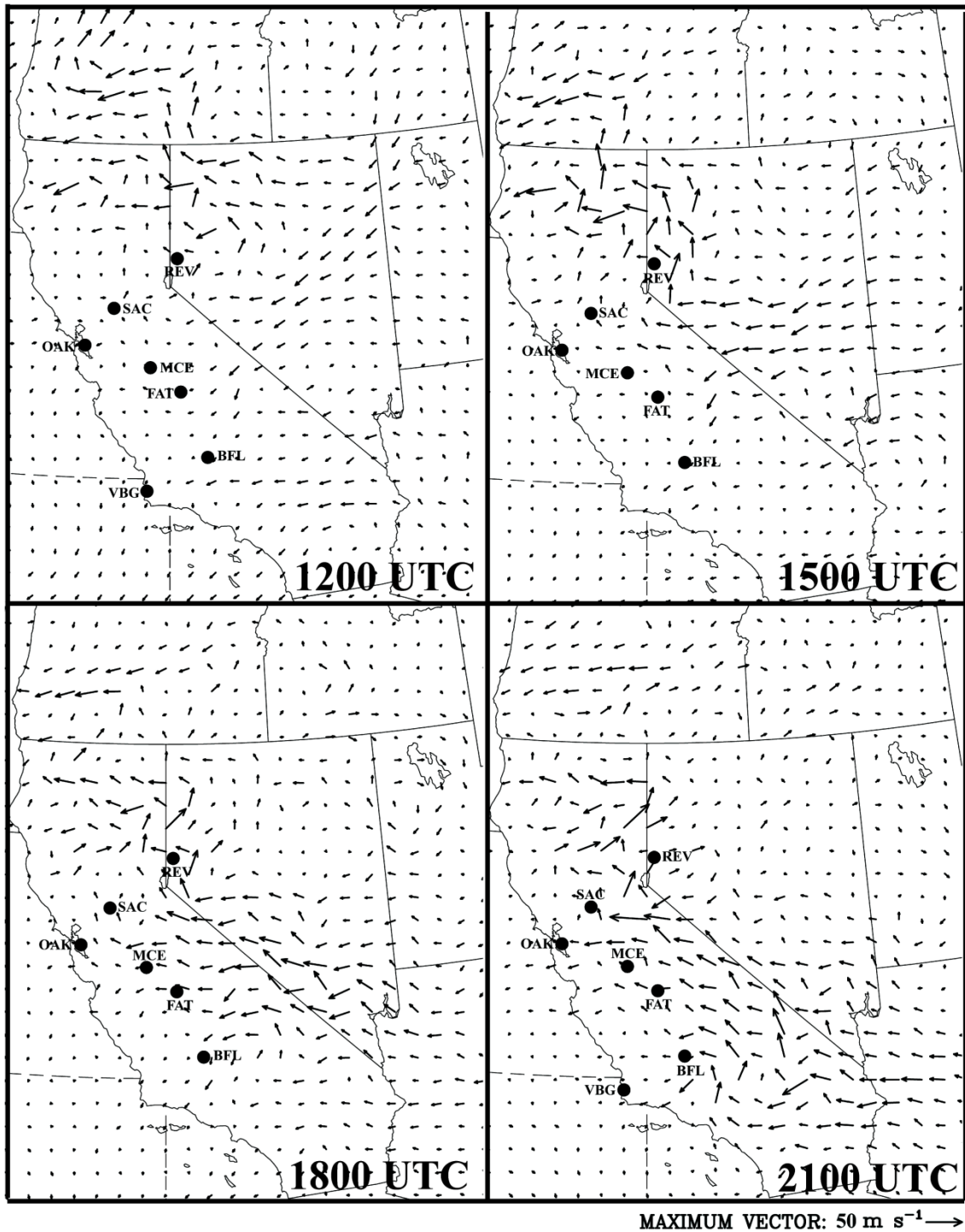


Figure 10. Ageostrophic wind vectors at 500 hPa diagnosed from 6-km WRF forecasts at 1200, 1500, 1800 and 2100 UTC 29 November 1991.

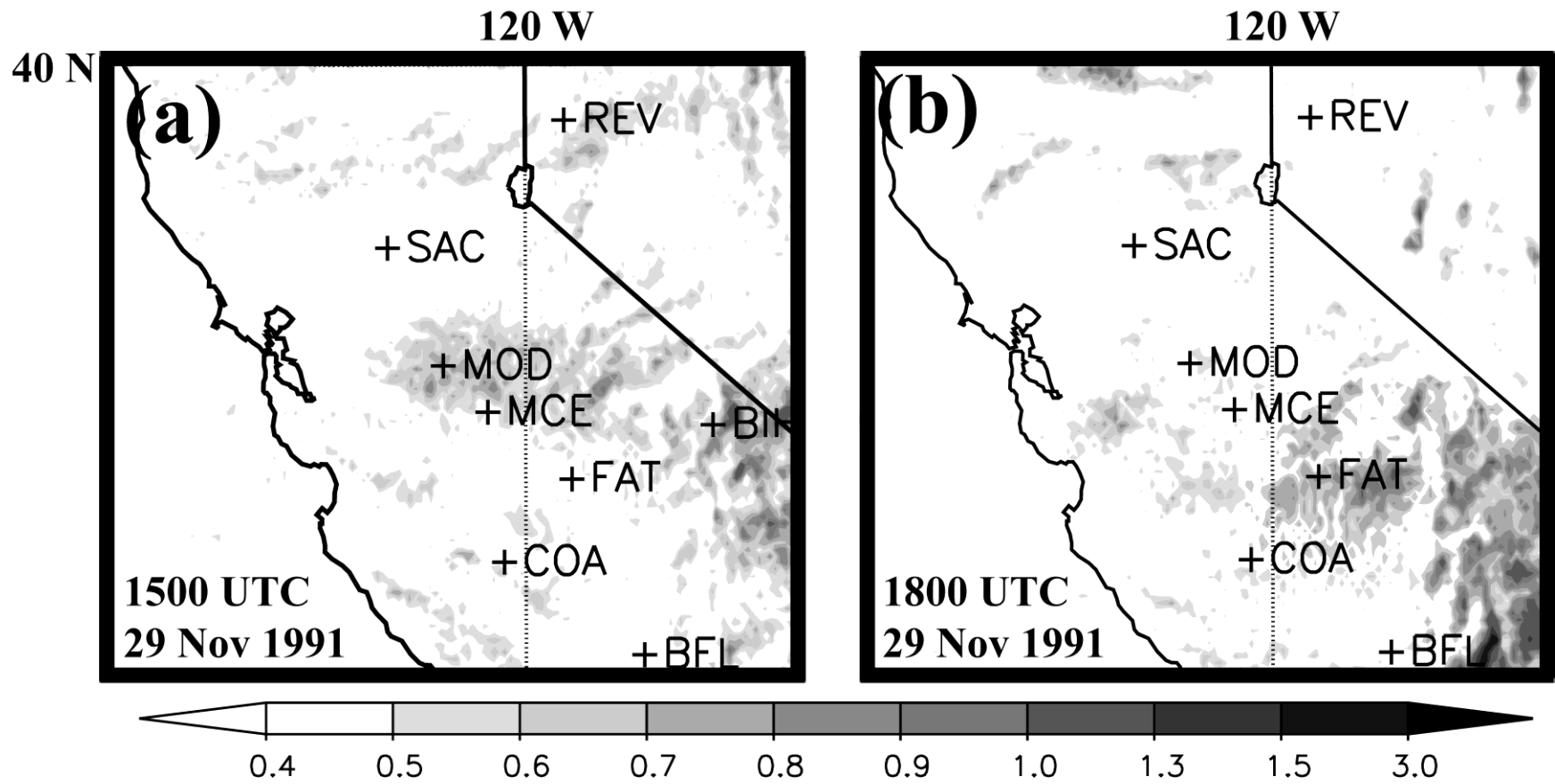


Figure 11. 2-km WRF diagnosed Lagrangian Rossby number (Ro^L) at 500 hPa valid for (a) 1500 and (b) 1800 UTC 29 November 1991. Locations of the stations REV, SAC, MOD, MCE, FAT, COA, BFL (see Table 1) are shown on the figure.

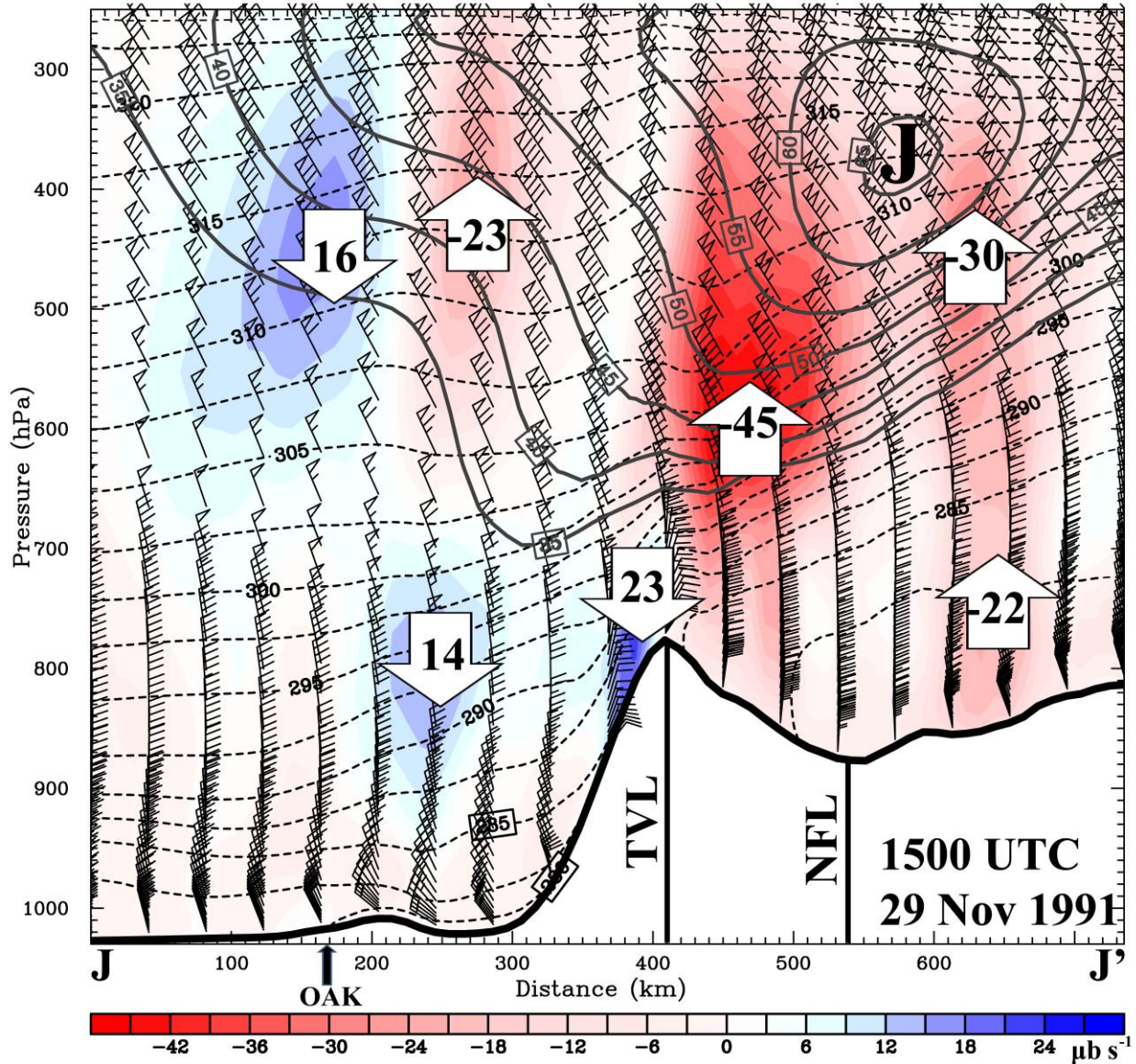


Figure 12. 18 km WRF simulated potential temperature (dashed; contour interval = 2 K), horizontal winds (full barb = 5 m s⁻¹), wind speeds (solid; contour interval = 5 m s⁻¹), vertical p-velocity (ω) (shaded; red = upward; blue = downward; $\mu\text{b s}^{-1}$) at 1500 UTC 29 November 1991 along the cross section J-J' shown in Figure 2. Magnitudes of vertical motion are indicated inside the arrows. Overlain in the figures are the total wind jet maximum (J) and locations of OAK and NFL along the cross section.

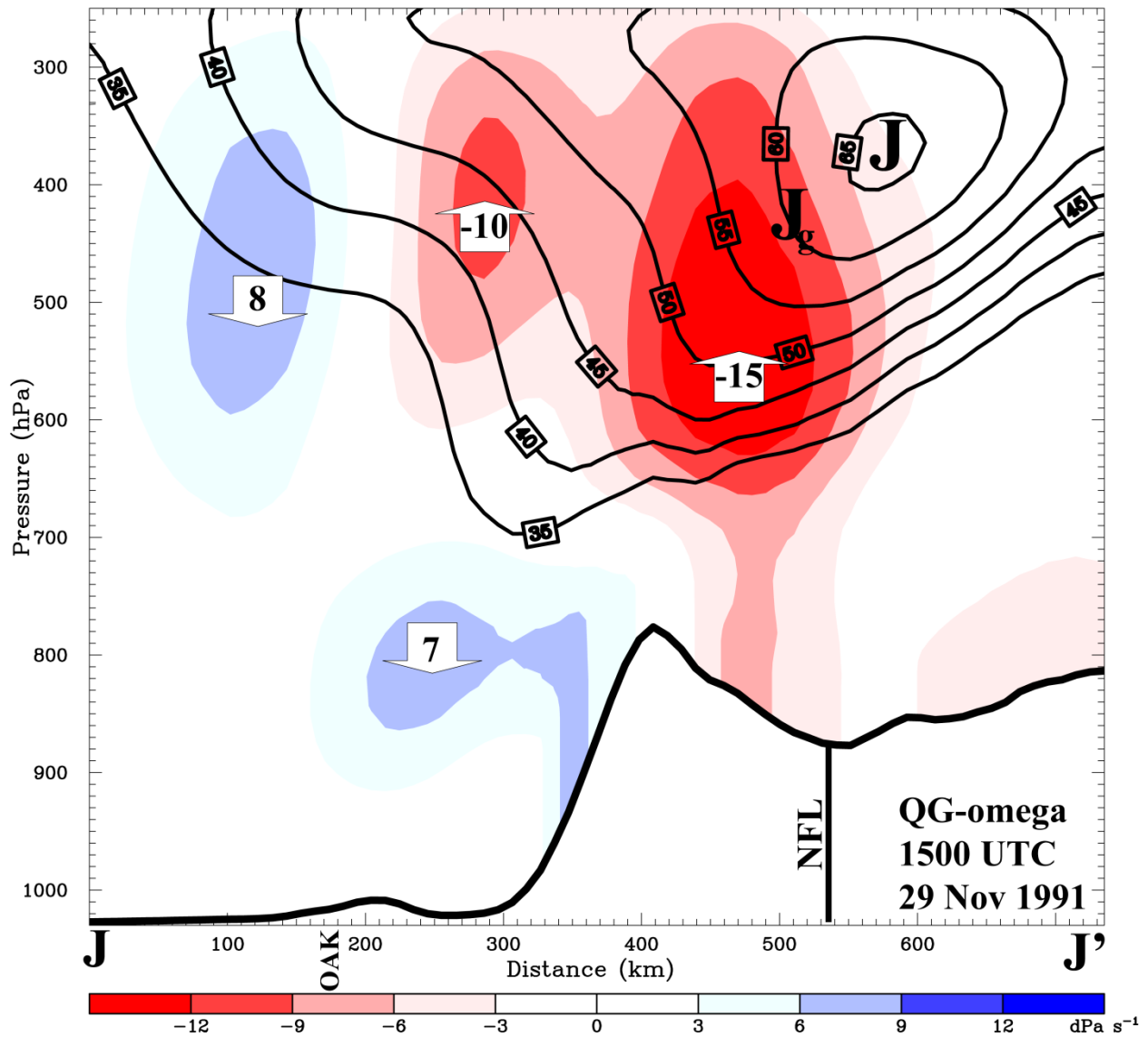


Figure 13. 18 km WRF simulated wind speeds (solid; contour interval = 5 m s⁻¹), diagnosed quasi-geostrophic vertical p-velocity (QG- ω) (shaded; red = upward; blue = downward; $\mu\text{b s}^{-1}$) at 1500 UTC 29 November 1991 along the cross section J-J' shown in Figure 2. Magnitudes of vertical motion are indicated inside the arrows. Overlain in the figures are the total wind jet maximum (J), geostrophic wind jet maximum (J_g) and locations of OAK and NFL along the cross section.

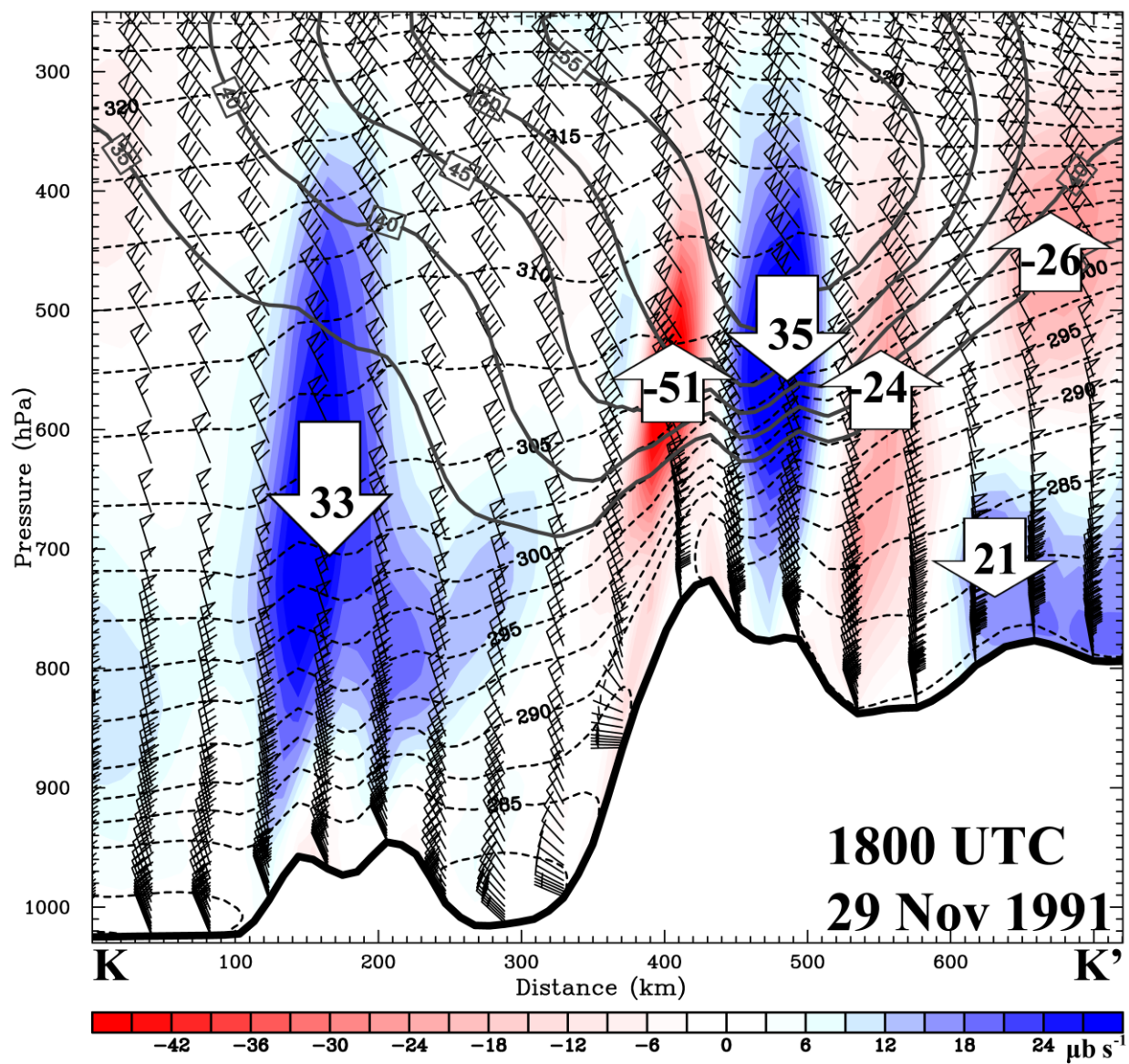


Figure 14. Same as described in Figure 12, but along the cross section K-K' (see Figure 2 for the orientation of the cross section) valid at 1800 UTC 29 November 1991.

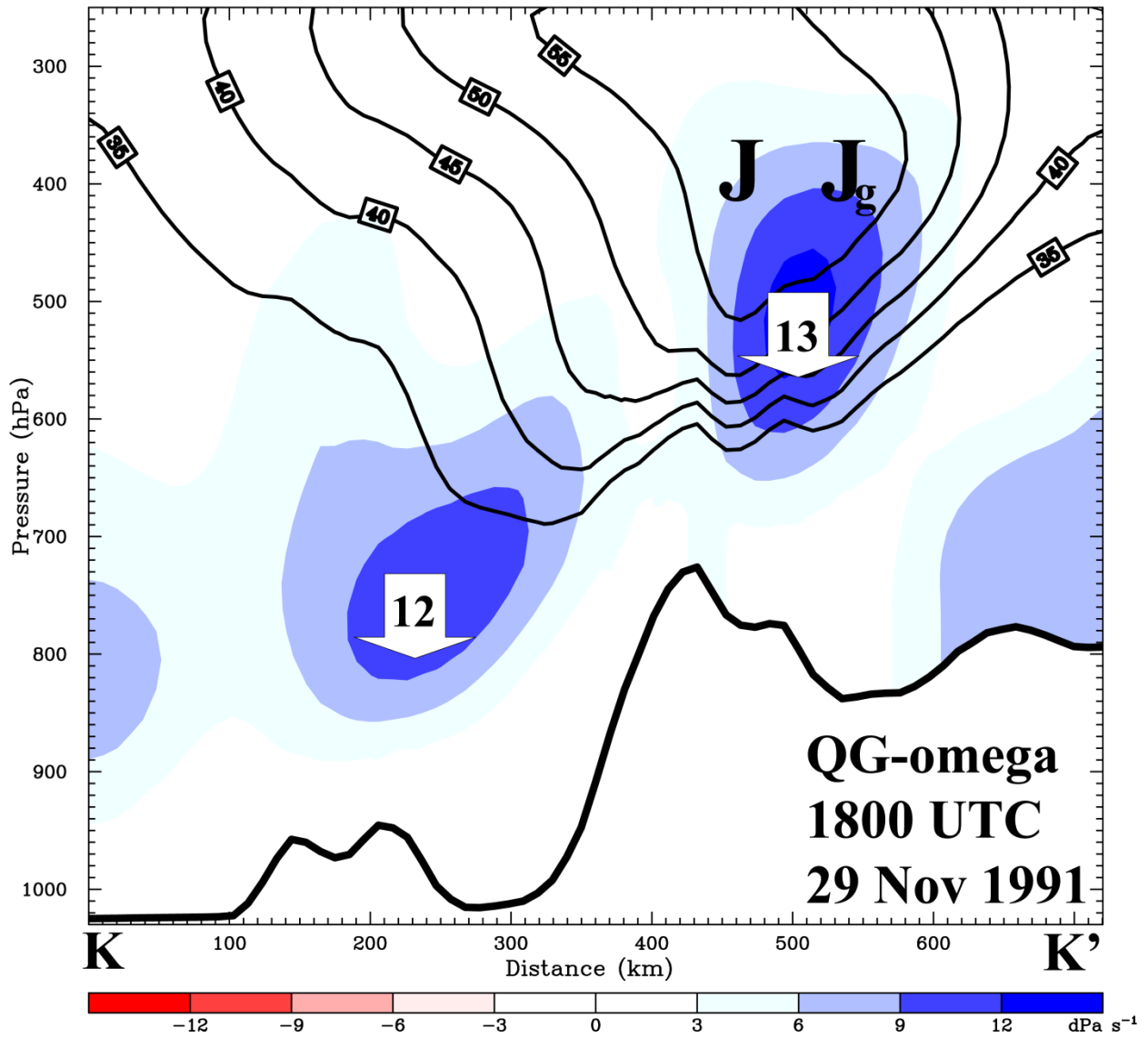


Figure 15. Same as described in Figure 13, but along the cross section K-K' (see Figure 2 for the orientation of the cross section) valid at 1800 UTC 29 November 1991.

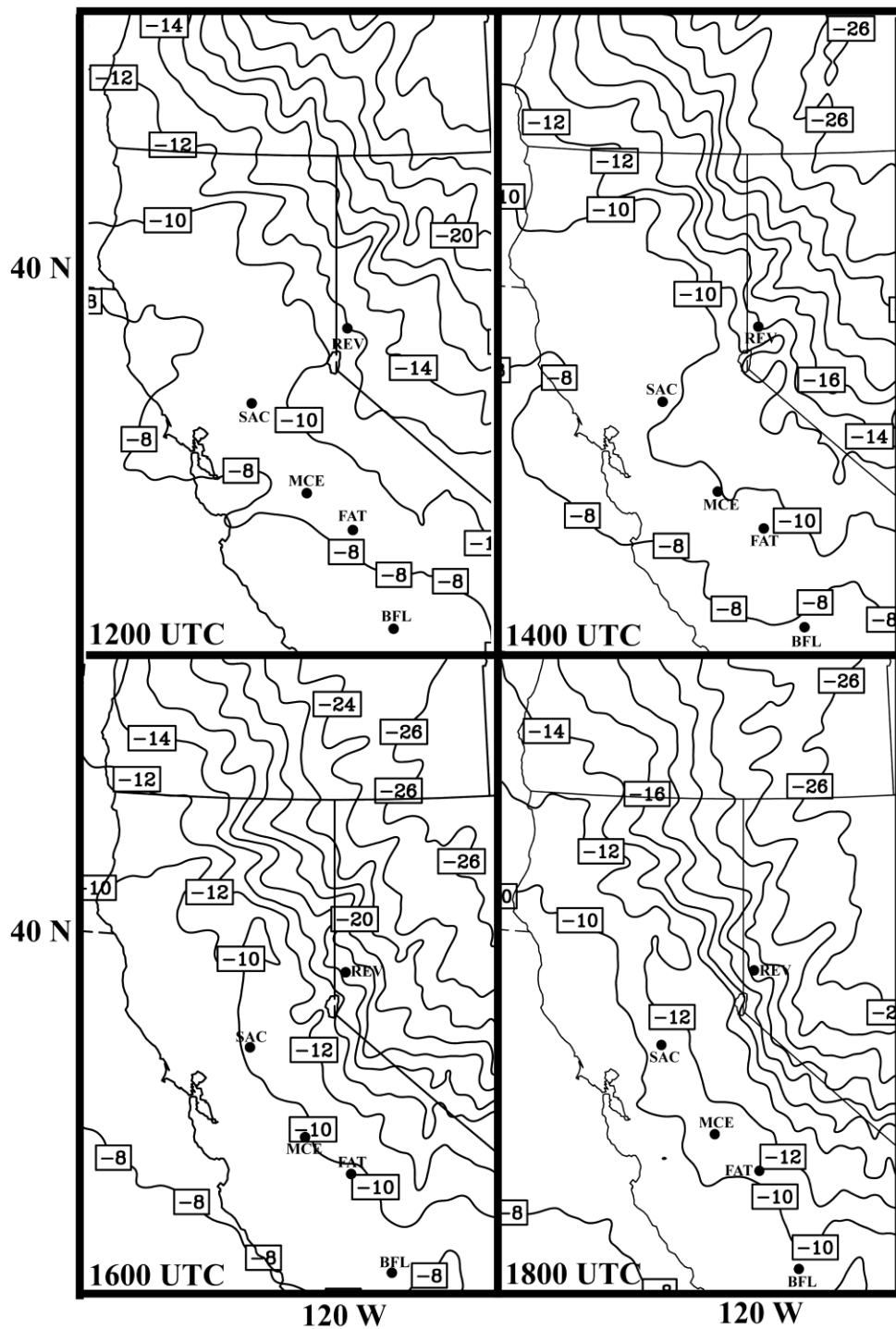


Figure 16. 2-km WRF diagnosed mean temperature (contour interval = 2°C) in the 500 – 700 hPa layer valid at 1200, 1400, 1600 and 1800 UTC 29 November 1991.

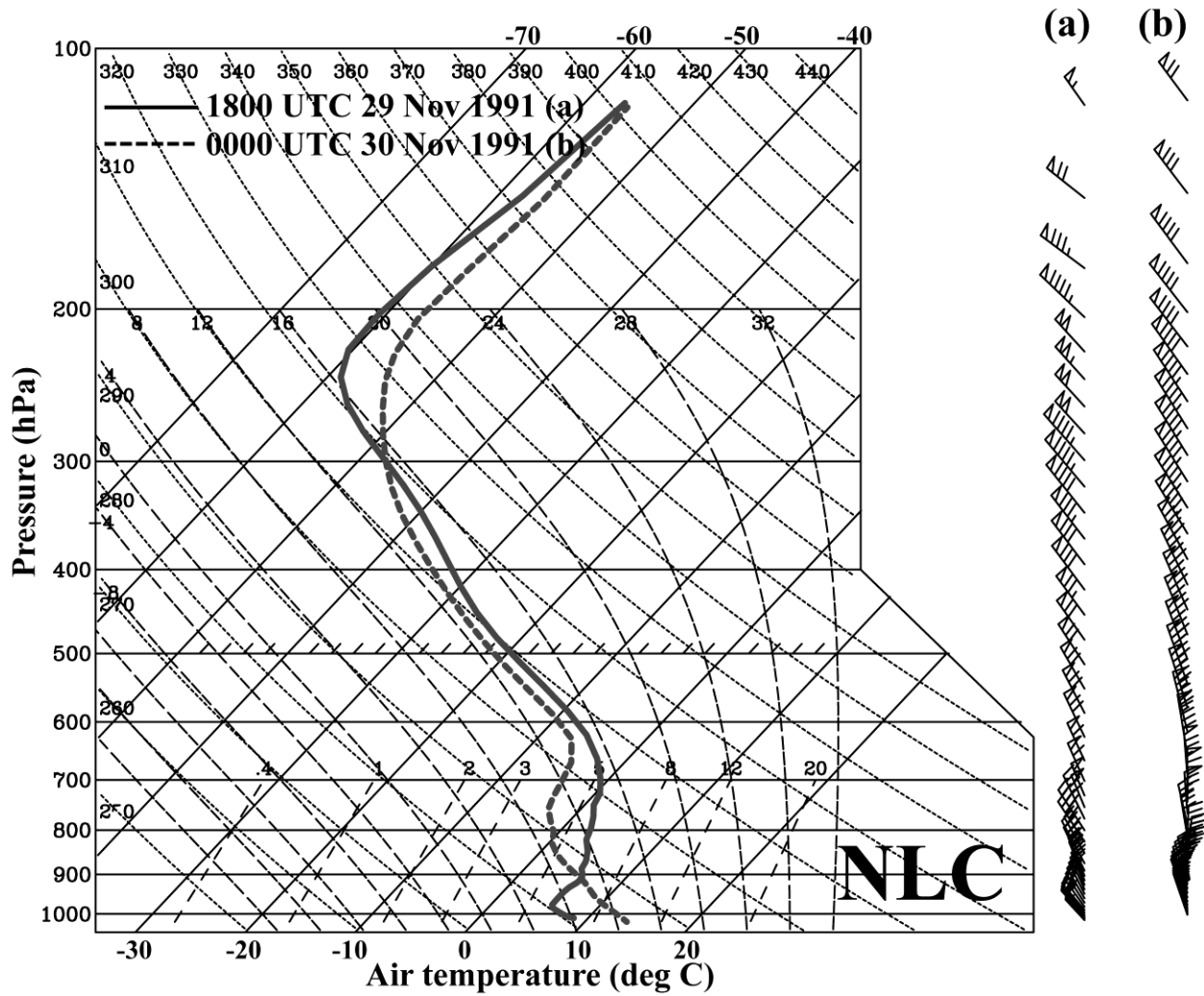


Figure 17. 2-km WRF simulated profiles of air temperature ($^{\circ}\text{C}$) and horizontal winds (full barb = 5 m s^{-1}) at Lemoore (NLC) and Bakersfield (BFL), California valid at (a,c) 1800 UTC 29 November 1991, and (b,d) 0000 UTC 30 November 1991.

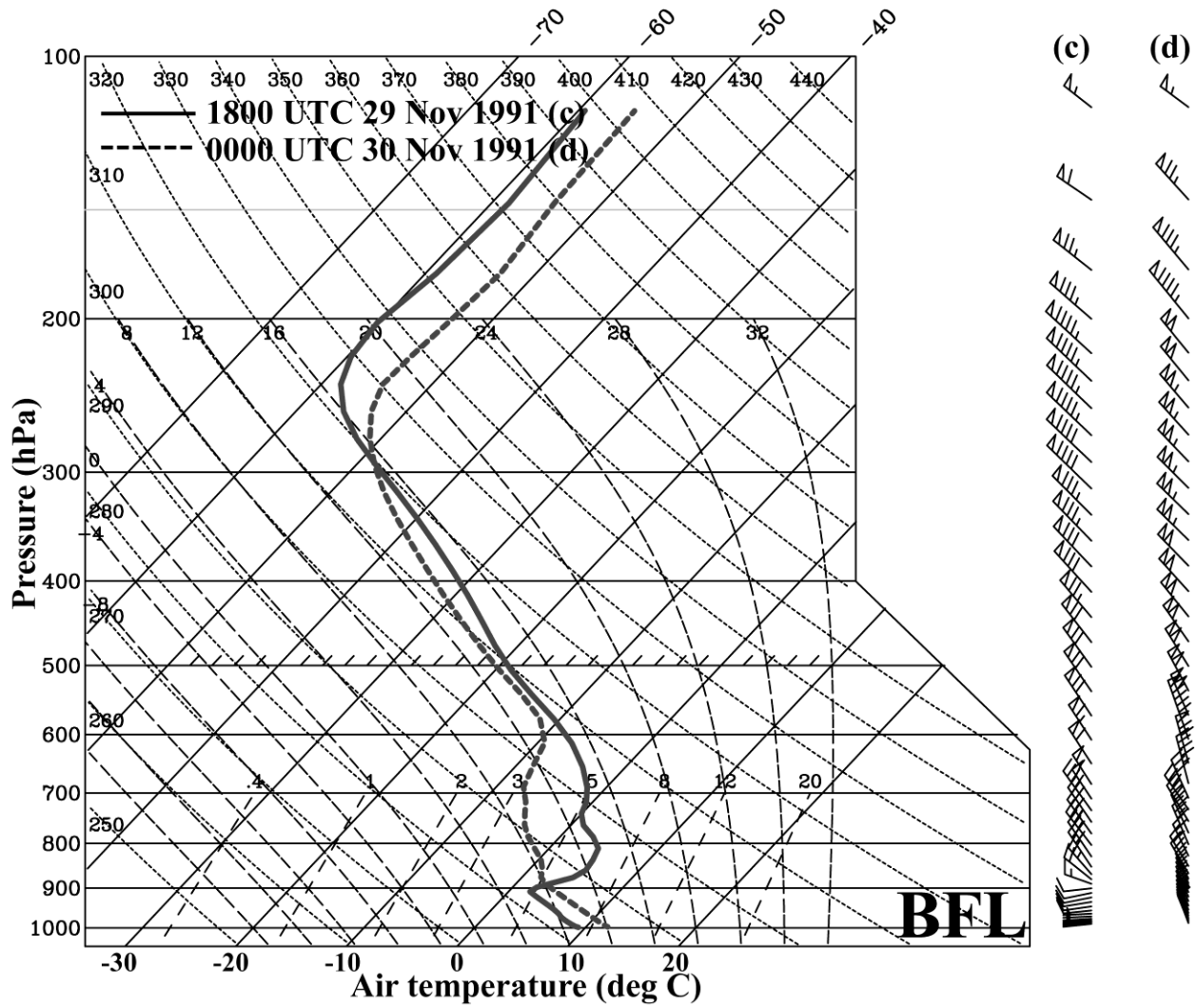


Figure 17. Continued.

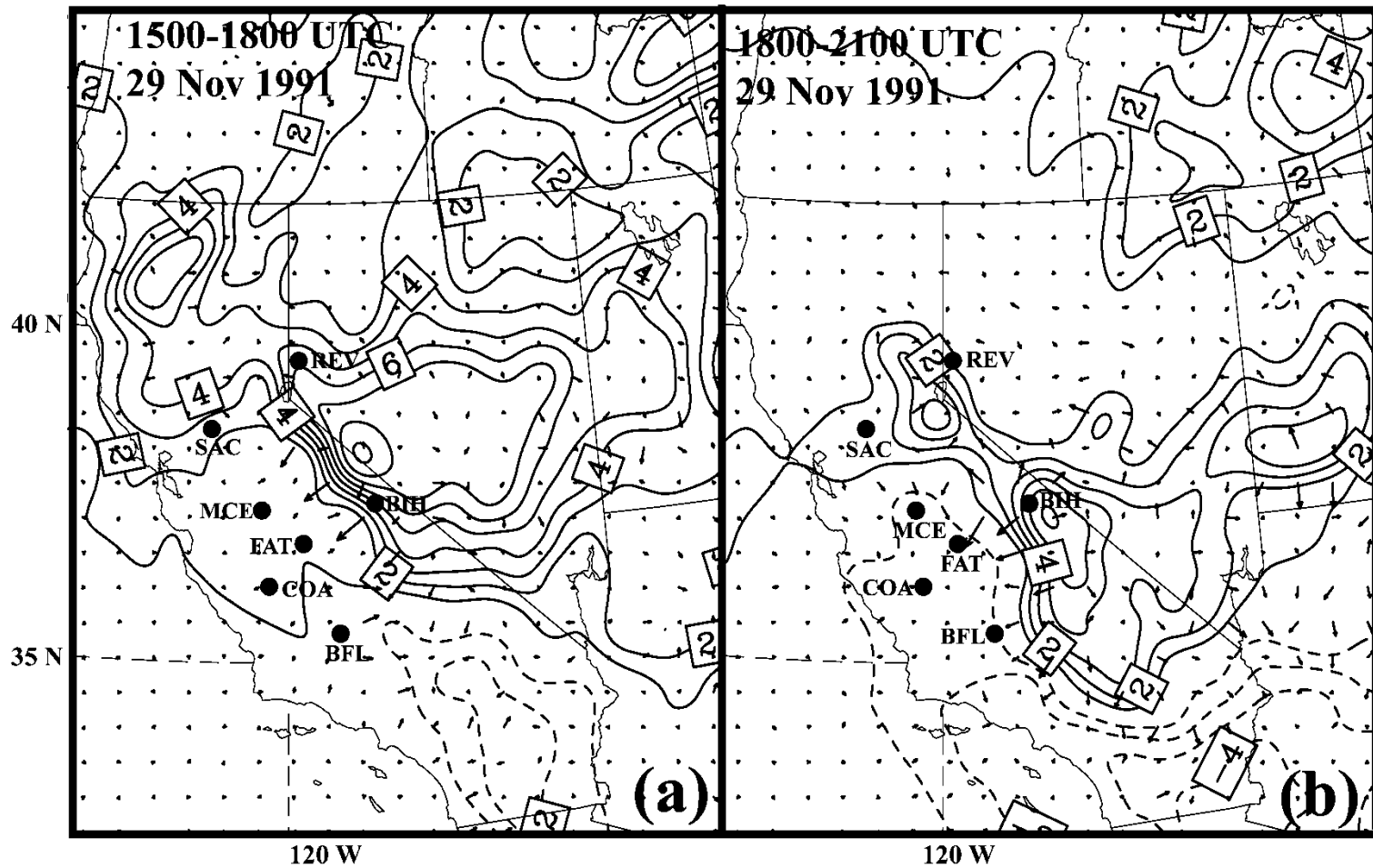


Figure 18. 6 km WRF diagnosed isallobaric winds (normalized vector lengths) from the 3-h mean sea level pressure tendency [contour interval = 1 mb] during (a) 1500-1800 UTC and (b) 1800-2100 UTC 29 November 1991. Locations of SAC, MCE, FAT, BIH, COA, BFL, and REV are shown in the figure.

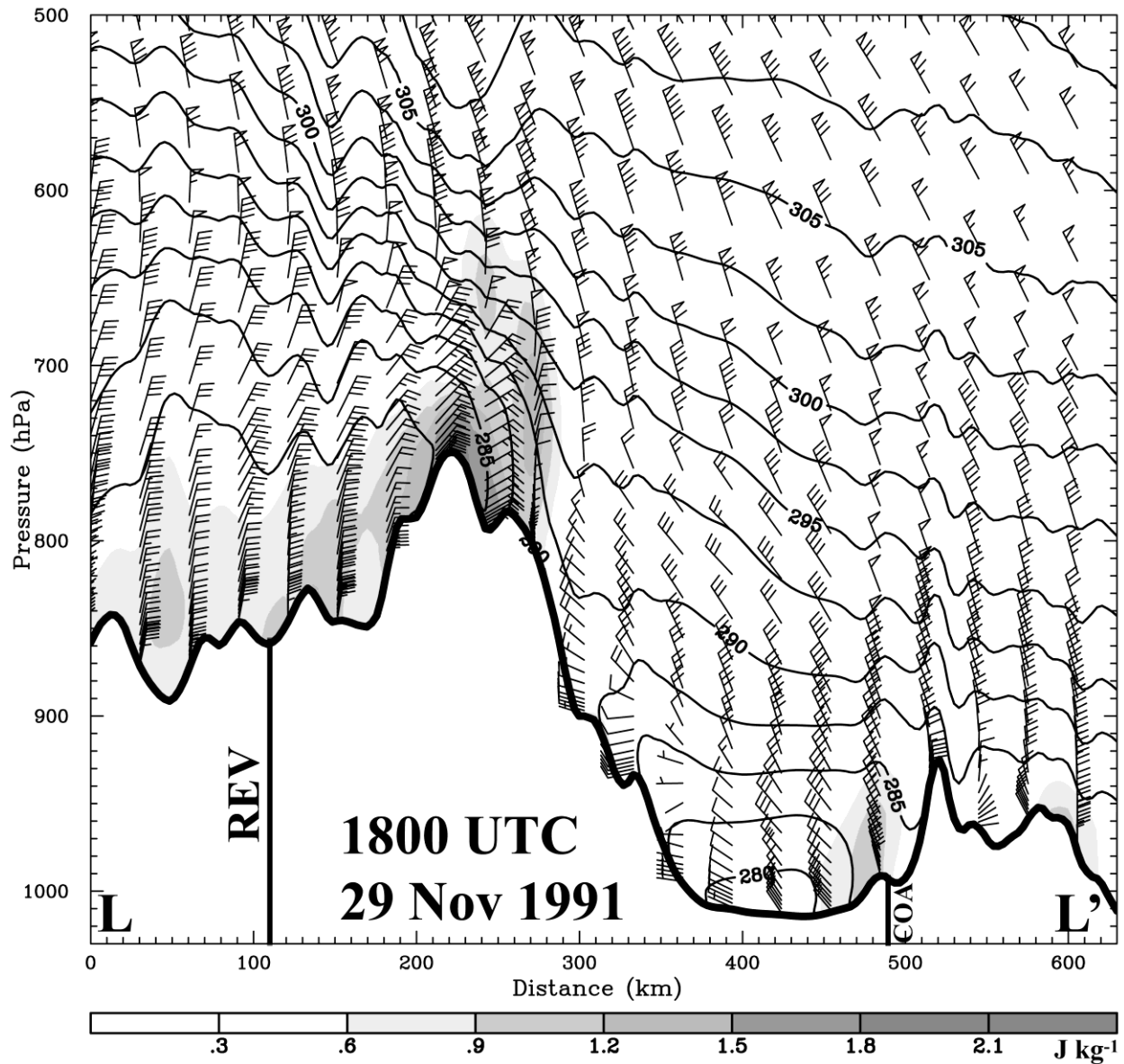


Figure 19. 6 km WRF simulated TKE (shaded; J kg^{-1}), horizontal winds (full barb = 5 m s^{-1}), potential temperature (solid; contour interval = 2.5 K) along the cross section L-L' (shown in Figure 2) at 1800 UTC 29 November 1991. Nearest locations to Reno (REV) and Coalinga (COA) are shown on the figure.

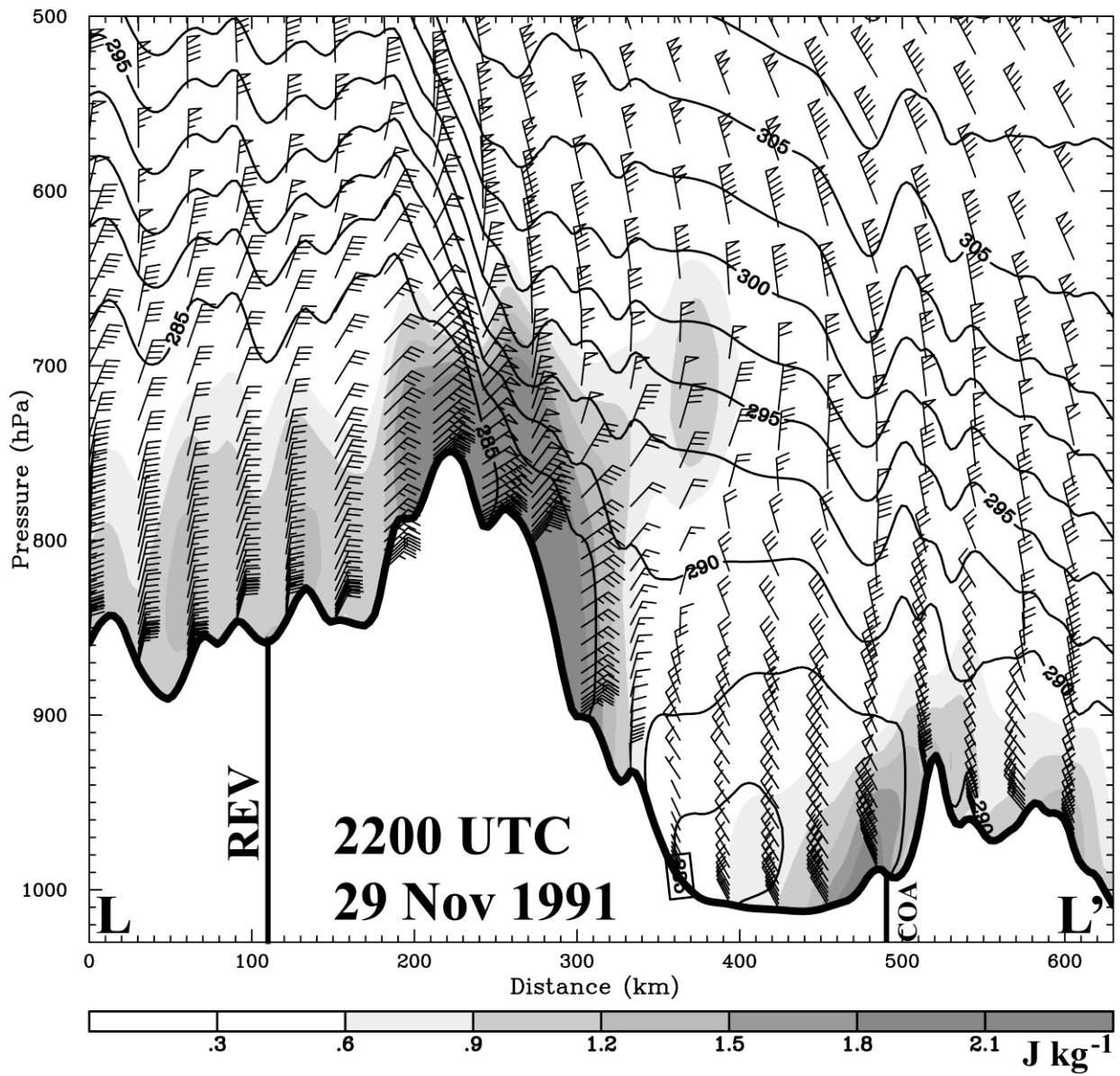


Figure 20. Same as in Figure 19, but valid at 2200 UTC 29 November 1991.

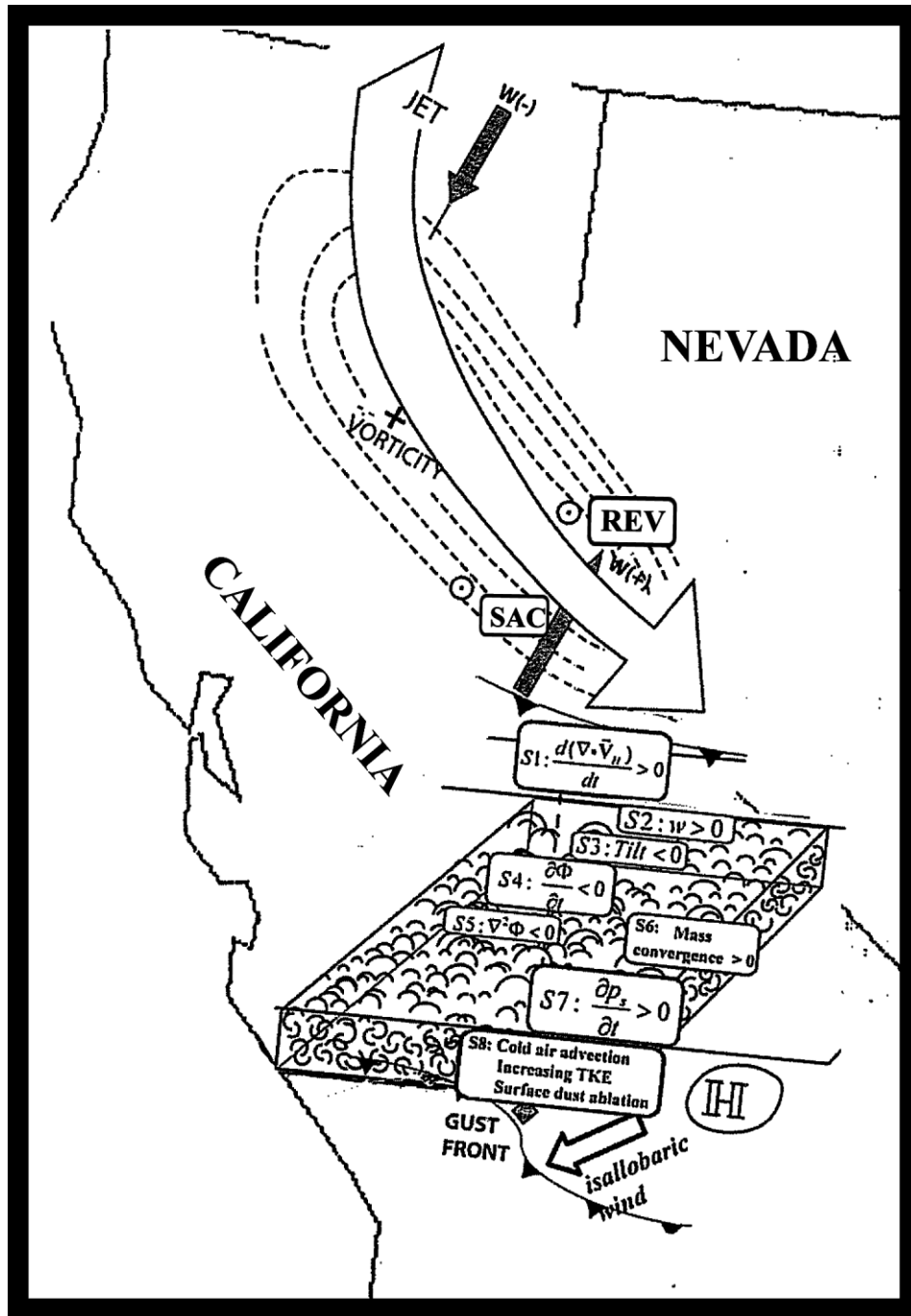


Figure 21. Schematic of the unbalanced circulations and fast adjustment signals during 1500 UTC 29 November 1991 – 0000 UTC 30 November 1991.